CellPress

Cell Chemical Biology

Article

CETSA interaction proteomics define specific RNA-modification pathways as key components of fluorouracil-based cancer drug cytotoxicity

Ying Yu Liang,[1,2,3,10] Smaranda Bacanu,[2,10] Lekshmy Sreekumar,[3] Anderson Daniel Ramos,[2] Lingyun Dai,[1,3,9] Martin Michaelis,[4] Jindrich Cinatl,[5] Takahiro Seki,[6,7] Yihai Cao,[6] Cynthia R. Coffill,[8] David P. Lane,[8] Nayana Prabhu,[1,3] and Pär Nordlund[1,2,3,11,*]

[1]Institute of Molecular and Cell Biology, A*STAR, Singapore 138673, Singapore
[2]Department of Oncology and Pathology, Karolinska Institutet, 171 77 Stockholm, Sweden
[3]School of Biological Sciences, Nanyang Technological University, Singapore 637551, Singapore
[4]School of Biosciences, University of Kent, Canterbury CT2 7NJ, UK
[5]Institute for Medical Virology, Goethe-University, Frankfurt am Main, Germany
[6]Department of Microbiology, Tumour and Cell Biology, Karolinska Institutet, 171 77 Stockholm, Sweden
[7]Kagoshima University Graduate School of Medical and Dental Sciences 8 Chome-35-1 Sakuragaoka, Kagoshima 890-8520, Japan
[8]p53Lab, A*STAR, 8A Biomedical Groove, Immunos, #06-06, Singapore 138648, Singapore
[9]Present address: The Second Clinical Medical College of Jinan University, the First Affiliated Hospital of Southern University of Science and Technology, Shenzhen People's Hospital, Shenzhen 518020, China
[10]These authors contributed equally
[11]Lead contact
*Correspondence: par.nordlund@ki.se
https://doi.org/10.1016/j.chembiol.2021.06.007

SUMMARY

The optimal use of many cancer drugs is hampered by a lack of detailed understanding of their mechanism of action (MoA). Here, we apply a high-resolution implementation of the proteome-wide cellular thermal shift assay (CETSA) to follow protein interaction changes induced by the antimetabolite 5-fluorouracil (5-FU) and related nucleosides. We confirm anticipated effects on the known main target, thymidylate synthase (TYMS), and enzymes in pyrimidine metabolism and DNA damage pathways. However, most interaction changes we see are for proteins previously not associated with the MoA of 5-FU, including wide-ranging effects on RNA-modification and -processing pathways. Attenuated responses of specific proteins in a resistant cell model identify key components of the 5-FU MoA, where intriguingly the abrogation of TYMS inhibition is not required for cell proliferation.

INTRODUCTION

Many drugs in clinical use lack a complete understanding of their mechanism of action (MoA) (Ledford, 2019; Lin et al., 2019). This hampers efforts toward grasping the underlying causes for adverse events, as well as work aimed at optimizing therapeutic efficacy for individuals and patient populations. Antimetabolite-based cancer drugs, including nucleoside and folate analogs, play critical roles in the therapy of many cancers (Luengo et al., 2017), as well as in immune and inflammatory diseases (Cronstein and Aune, 2020; Taylor et al., 2019). However, they often display complex responses and broad toxicities, and few robust biomarkers of therapeutic efficacy and toxicity exist for these drugs.

5-Fluororuracil (5-FU), an analog of uracil, is a classic antimetabolite chemotherapeutic agent that has been the first-line treatment of colorectal cancer since the 1960s (Showalter et al., 2008). 5-FU and its prodrug capecitabine are also used for various other cancers such as breast cancer (Deveci et al., 2018), pancreatic cancer (McGuigan et al., 2018), lung cancer (Nakano et al., 2006; Pan et al., 2013), and head and neck cancer (Longley et al., 2003). Even though 5-FU has been used for more than half a century in cancer therapy, its MoA is only partially understood. After entering cells, 5-FU is converted into the nucleoside metabolites 5-fluorouridine (FUR) and 5-fluorodeoxyuridine (FUDR) (Christensen et al., 2019; Grem, 2000; Vodenkova et al., 2020). Both compounds constitute key metabolites of 5-FU, differing only in the structure of their ribose moieties (Figure 1A), and FUDR is also approved for use in, for example, colorectal cancer. FUR and FUDR are subsequently phosphorylated by cellular nucleoside kinases (Figure 1D). Thymidylate synthase (TYMS) has been considered the major protein target of 5-FU and FUDR (and metabolized FUR), and is inhibited by the FUDR monophosphate metabolite (FdUMP). TYMS is the only pathway for *de novo* synthesis of thymidine monophosphate (dTMP) in cells, and depletion of cellular thymidine nucleotides leads to imbalanced deoxynucleotide pools and subsequent misincorporation of uracil during DNA synthesis and repair. Fluorouridine triphosphate (FUTP) and fluorodeoxyuridine triphosphate (FdUTP) are other key metabolites of 5-FU and can be

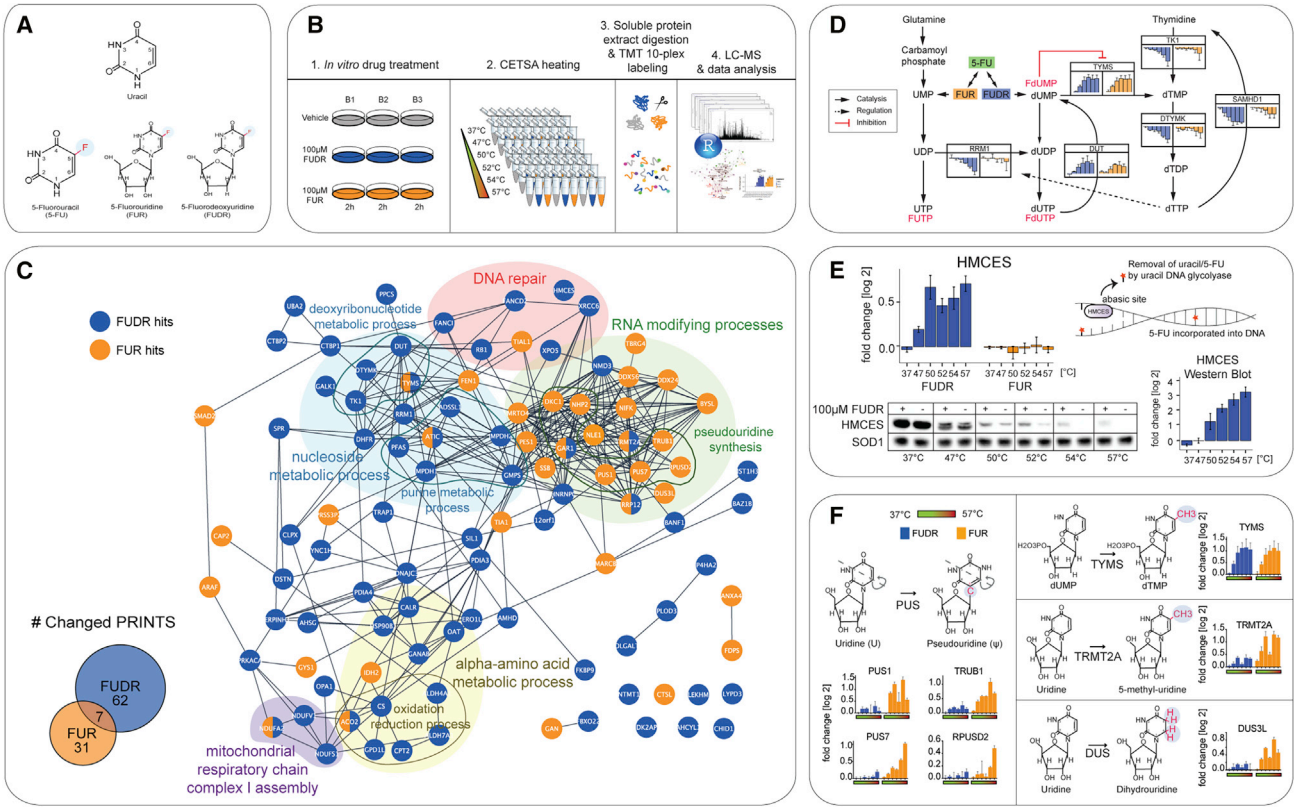

Figure 1. Early FUDR and FUR CETSA responses display orthogonal pathway effects

(A) Chemical structures of uracil, 5-FU, FUR, and FUDR.

(B) Experimental outline of IMPRINTS-CETSA.

(C) Left: Venn diagram represents the number of proteins with changed PRINTS after FUDR (blue) and FUR (orange) treatment. Right: STRING analysis of protein hits after FUDR and FUR treatment. Nodes represent changed protein hits upon FUDR or FUR treatment. Clusters of interest are highlighted in different background colors.

(D) Schematic view of dNTP *de novo* synthesis pathway and the CETSA effect of FUDR and FUR on key proteins. Data are presented as mean $\log_2$ fold change compared to the reference ±SEM from biological replicates (n = 3).

(E) Top left: IMPRINTS profiles for HMCES obtained from LC-MS shows thermal stabilization only in FUDR but not FUR treatment. Top right: graphical depiction of HMCES-DNA interaction illustrates that misincorporated 5-FU (or uracil) in DNA is removed by uracil DNA glycosylase, leading to an abasic site in DNA. Bottom: reproducible WB-CETSA confirms HMCES thermal stabilization with a profile similar to that of the LC-MS IMPRINTS. Data are presented as mean $\log_2$ fold change compared to the reference ±SEM from biological replicates (n = 3).

(F) Reaction of 5xU modifying enzymes TYMS, TRMT2A, DUS3L, and Ψ-synthase family members PUS1, PUS7, RPUSD2, and TRUB1. IMPRINTS profiles show effect of FUDR or FUR on thermal stability. Data are presented as mean $\log_2$ fold change compared to the reference ±SEM from biological replicates (n = 3).

misincorporated into RNA and DNA, respectively. Other intermediate products (FUMP, FUDP, and FdUDP) may have additional effects on the nucleotide metabolism pathway. Molecular and cellular effects of thymidine depletion, 5-FU and uracil misincorporation into DNA/RNA, as well as diverse effects on metabolic and signaling pathways, have been studied as potential components of the 5-FU MoA (Vodenkova et al., 2020). However, a comprehensive understanding of the direct cellular effects induced by 5-FU and how these differentially contribute to downstream events, including cell-cycle arrest and apoptosis, is still missing. Similarly, mechanistic knowledge of 5-FU resistance also remains incomplete. Despite initial clinical responses after 5-FU treatment, patients often relapse and acquired resistance is a major cause of death in, e.g., colorectal cancer (Kuipers et al., 2015; Sobrero et al., 1997). Most efforts toward understanding 5-FU resistance have been focused on evaluating the expression levels of TYMS as well as enzymes involved in drug activation and catabolism (Iyevleva et al., 2007; Qiu et al., 2008; Zhang et al., 2008). Although some significant correlations to drug efficacy and resistance have been found, they have not yielded sufficiently robust biomarkers for guided therapy (Van Der Jeught et al., 2018; Sasada et al., 2013).

Due to the complexity of cellular effects induced by 5-FU and other antimetabolites, a systems approach is arguably needed for a comprehensive understanding of the proteins and pathways involved in different stages of their MoA. Transcriptomics and proteomics have been applied to assess cellular effects of 5-FU (Iacovides et al., 2018; Marin-Vicente et al., 2013; Rodrigues et al., 2019; Tieng et al., 2020). However, these methods typically catch delayed effects, after transcriptional reprogramming, and miss the early molecular events underlying the drug response. These expression level-focused methods also miss

many of the cellular drug effects that only affect molecular interactions. The cellular thermal shift assay (CETSA) was recently introduced as the first broadly applicable method to study modulation of interactions with proteins directly in intact cells and tissues (Molina et al., 2013). The proteome-wide, mass-spectrometry-based implementation (MS-CETSA) has recently been demonstrated as a novel approach for comprehensive mapping of PRotein INTeraction States (PRINTS), i.e., interaction changes in the proteome during cellular processes and drug action (Dai et al., 2018, 2019; Prabhu et al., 2020).

In the present work we explore the recently implemented high-resolution IMPRINTS (Integrated Modulation of PRINTS)-CETSA for studies of cellular effects of 5-FU, FUDR, and FUR. The results reveal comprehensive modulations of many different proteins and pathways by these drugs at different time points. While several of the proteins involved in the 5-FU MoA were previously shown to be affected by fluorouracil compounds, thus validating our approach, most of them are previously not implicated players. Intriguingly, in resistant colon cancer cells we show that TYMS is still engaged and likely inhibited by 5-FU metabolites, while other direct interactions in parental cells are attenuated. We also show that RNA-derived effects are dominant features of the 5-FU MoA and stringent inducers of p53 activation. The study therefore provides a distinct perspective on the critical determinants for the MoA of 5-FU-based compounds, including specifically targeted enzymes in RNA-modification pathways that can also serve as biomarkers for drug efficacy.

RESULTS

Early FUDR and FUR CETSA responses display orthogonal pathway effects

Understanding early molecular events is essential in determining the MoA of drugs, as they define subsequent cellular effects. 5-FU is relatively slowly activated in cells (Almqvist et al., 2016); therefore, we first assessed the early effects of its metabolites, FUDR and FUR on the proteome with MS-CETSA. We reasoned that early responses of these two drugs could, in addition to shedding light on their MoA, allow us to dissect DNA-versus-RNA specific effects of fluorouracil-based drugs. For optimal sensitivity we explored IMPRINTS-CETSA (Dai et al., 2018, 2019) as outlined in Figure 1B. When performing IMPRINTS-CETSA for cancer drugs, we selected a compound concentration that is well tolerated by the cells, i.e., with little effect on viability in the conditions used up to the maximum time point selected for the IMPRINTS-CETSA experiment but where, after a longer exposure time (typically 2–3 days), a significant cytotoxic effect (efficacy) was observed. Based on this strategy, MCF7 cells were treated with either 100 μM FUDR, 100 μM FUR, or vehicle for 2 h to capture early cellular changes before extensive transcriptional responses were affected. At these drug concentrations, 98% (for FUDR) and 97% (for FUR) of cells were still viable at 2 h while a significant fraction of cells (~50%) were dying or had stopped dividing at 48 h (Figure S1A). Cells were subsequently harvested and subjected to CETSA heating and sample processing followed by liquid chromatography-mass spectrometry (LC-MS), data collection and analysis. Data statistics are summarized in Table S1. When compared with vehicle control, 69 and 38 proteins show changed PRINTS for FUDR and FUR treatment, respectively, with only seven common hits between these two drugs (Figure 1C) and TYMS showing the strongest shift while similarly affected in both treatments (Figure S1B). Comparative gene ontology (GO) analysis revealed CETSA effects of each of these fluorouracil-based drugs on distinct orthogonal cellular pathways, as shown in Figure 1C. FUDR treatment had major effects on diverse nucleoside processing pathways or DNA repair proteins, cellular processes related to amino acid metabolism, and mitochondrial respiratory chain assembly, while FUR predominantly induced shifts in proteins related to RNA-modification and processing.

A dominant feature of the FUDR response is the effect on deoxypyrimidine metabolism. While TYMS is stabilized, several key enzymes in thymidine metabolism (TK1, DTYMK, RRM1, SAMHD1) are destabilized (Figure 1D). These enzymes engage in interactions with different thymidine metabolites as substrates, products, or allosteric regulators in the cell, and thus the destabilization likely reflects decreased thymidine nucleotide levels, in accordance with previous CETSA studies (Dai et al., 2018; Lim et al., 2018). We also observed a stabilization in DUT, the dUTPase catalyzing the dUTP → dUMP transformation. To investigate whether fluorouracil metabolite binding to DUT could be directly detected with CETSA, we explored western blot (WB)-based isothermal dose response CETSA (ITDR$_{CETSA}$) with FdUTP or FdUMP in cell lysate (Figure S2A). We observed an apparent high-affinity thermal stabilization of DUT following FdUTP exposure and a lower affinity binding of FdUMP, consistent with previous proposals that FdUTP is a substrate for DUT (Caradonna and Cheng, 1980; Sakamoto et al., 2015). We have previously demonstrated that DUT is stabilized by dUMP (Lim et al., 2018); therefore, the stabilization of DUT could reflect either the accumulation of deoxyuridine metabolites (the substrate dUTP or the product dUMP) induced by TYMS inhibition, or the direct binding of FdUTP or FdUMP. In addition to pyrimidine pathways, several enzymes in the purine metabolism are also affected by FUDR treatment. These include enzymes such as IMPDH1, IMPDH2, and GMPS, as well as PFAS and ATIC (Figure 1C). These stability changes could reflect specific effects on the transport or metabolite flux in these pathways, induced as a secondary effect of the distortions in the pyrimidine metabolism.

Interestingly, FUDR treatment also led to thermal shifts in DNA repair-related proteins HMCES, FANCD2, FANCI, and XRCC6. The most prominent shift was observed for HMCES, which we also confirmed with WB-CETSA (Figure 1E). HMCES was recently shown to be a novel DNA repair protein that shields abasic sites in single-stranded DNA (ssDNA) during DNA repair (Mohni et al., 2019), and structural studies have confirmed covalent interactions between HMCES and DNA (Halabelian et al., 2019; Thompson, 2019). HMCES has not previously been associated with the 5-FU MoA. Our results suggest that such a protein-DNA interaction might be a consequence of (fluoro-)uracil misincorporation into DNA after FUDR treatment.

Many proteins in the early FUR response are involved in different RNA-modification processes (Figure 1F). Prominent CETSA stabilizations are seen for several members of the pseudouridine synthase family: PUS1, PUS7, TRUB1, and RPUSD2. These are isomerases converting specific uridines in mRNA, tRNA, rRNA, small nucleolar RNA (snoRNA), and other RNAs to

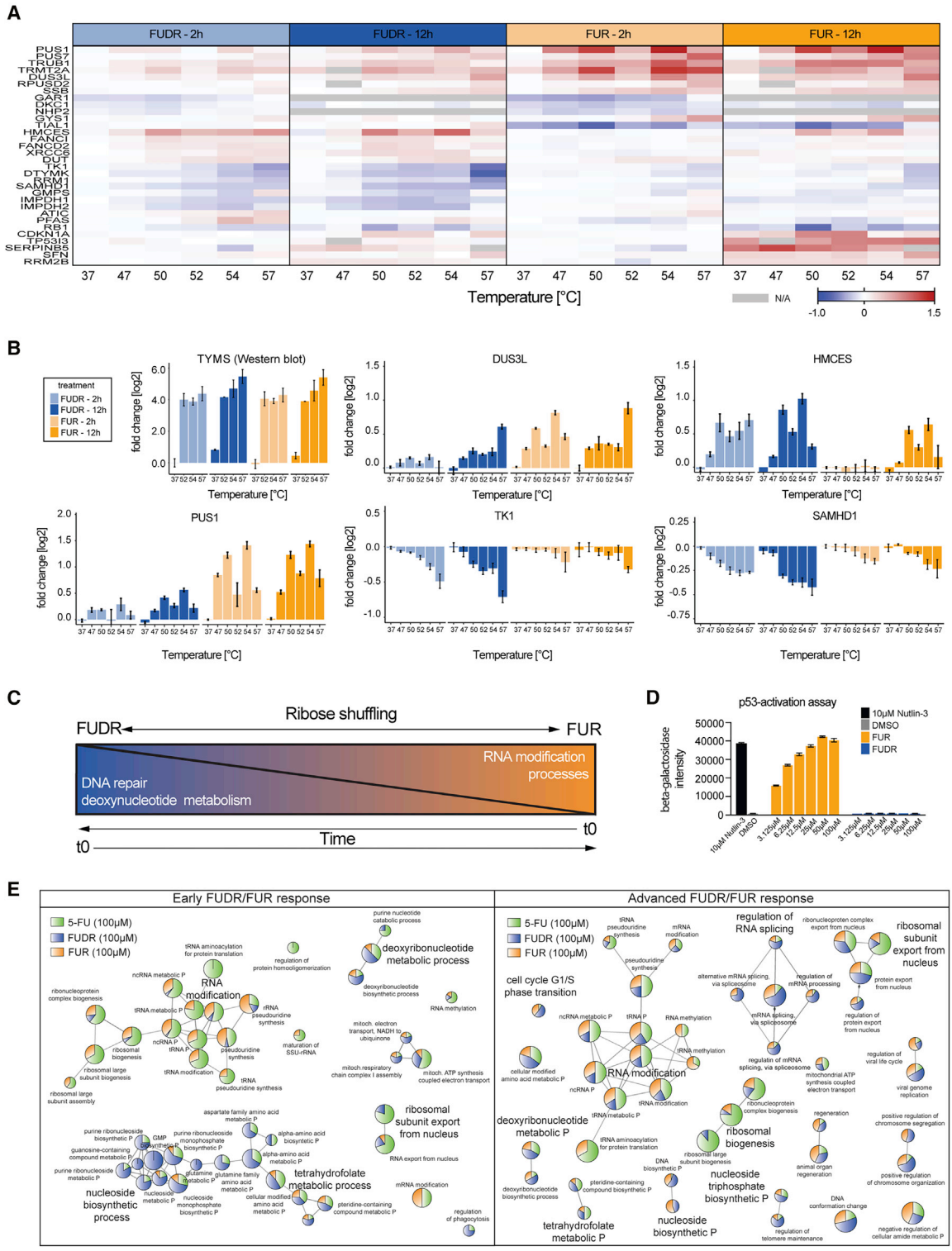

Figure 2. Time dependence of FUDR and FUR responses

(A) Heatmap showing the relative protein abundance and thermal stability changes (log_2) at the indicated temperatures for the proteins of interest.

(B) Examples of IMPRINTS profiles comparing FUDR (blue) and FUR (orange) at 2 h and 12 h from data collected with LC-MS. Data are presented as mean log_2 fold change compared to the reference ±SEM from biological replicates (n = 3). TYMS profile shown with WB analysis.

(C) Schematic illustration of "ribose shuffling." Over time, FUR and FUDR metabolites can be interconverted.

(D) p53-activation β-galactosidase reporter assay of ARN8 cells after 22 h of treatment with indicated concentrations of FUR, FUDR, Nutlin-3 (positive control), or dimethyl sulfoxide (negative control) (n = 3).

(legend continued on next page)

pseudouridine (Ψ), thereby affecting RNA stability and structure (Penzo et al., 2017). Ψ-synthases were previously shown to be directly involved in 5-FU response in *Caenorhabditis elegans* and oocytes (Zhao and Yu, 2007). 5-FU-modified tRNAs can covalently interact with Ψ-synthases through a catalytic Asp/Glu residue (Gu et al., 1999) to form an inhibitory complex. Due to the strong shifts in these Ψ-synthases and the fact that they use similar reaction mechanisms, it is likely that these reflect the formation of covalent complexes with cognate RNA that have been modified with fluorouracil. Another prominent CETSA stabilization in FUR-treated cells is seen for the tRNA uracil-5-methyltransferase TRMT2A, recently suggested to be a cell-cycle regulator (Chang et al., 2019). TRMT2A has been shown to form a covalent complex with 5-FU-modified tRNA in HEK293 cells and is suggested to play a role in 5-FU toxicity (Carter et al., 2019). DUS3L, which catalyzes the synthesis of dihydrouridine, also shows stabilization in FUR-treated cells. Dihydrouridine content in RNA is increased in tumor cells and has been suggested as a prognostic biomarker in lung cancer (Kato et al., 2005). This is an important demonstration of a potential role of a dihydrouridine synthase in the MoA of fluorouracil compounds. Interestingly, all the aforementioned stabilized RNA-interacting proteins, as well as TYMS, have a feature in common: they perform modifications on the fifth C-position on the uracil ring, i.e., they are 5xU-modifying proteins. It is possible that most of these yield covalent inhibitory complexes with 5-FU-modified RNA. Furthermore, we detected three subunits of the H/ACA ribonucleoprotein complex (DKC1, NHP2, and GAR1), having Ψ-synthase activity, that are destabilized (Figure 2A). This complex catalyzes pseudouridylation of rRNA and plays a role in ribosome biogenesis as well as in telomere maintenance (Penzo et al., 2017).

It is noteworthy that all the CETSA responses discussed above involve only thermal stability shifts, i.e., no or only small changes in protein levels are seen at 37°C. These shifts would therefore not be detectable with standard quantitative proteomics techniques.

Time dependence of FUDR and FUR responses

We also collected data at a 12 h time point for 100 μM FUDR or 100 μM FUR to study the time dependence of the shifts observed at 2 h (Figure 2A). TYMS was similarly engaged by FUDR and FUR after 12 h of treatment (Figure 2B, with WB-CETSA due to limited proteome sampling in MS data). In FUDR, many of the effects on proteins associated with nucleotide metabolism were maintained from 2 h to 12 h, including proteins sensitive to thymidine metabolite levels such as DTYMK, RRM1, TK1, and SAMHD1, as well as proteins involved in purine metabolism (GMPS, IMPDH1, and IMPDH2). Similar to FUDR, many of the strongly stabilized proteins in the 2 h FUR treatment had comparable or stronger IMPRINTS profiles at 12 h. These included the 5xU-modifying proteins PUS1, PUS7, TRUB1, DUS3L, TRMT2A, and RPUSD2. Lupus La protein (SSB), another RNA-binding protein known to be associated with 5xU-modified RNAs (Maraia and Intine, 2002), maintained its stabilization at both time points. Similarly, we observed comparable destabilized IMPRINTS profiles for TIAL1 at 2 h and 12 h. TIAL1 is a member of an RNA-binding protein family that recognizes and binds uridine-rich elements in mRNA, adding to fidelity of sensing RNA-induced stress (Meyer et al., 2018).

Notably, for some proteins that are shifted at 2 h in only either FUDR (e.g., HMCES) or FUR (e.g., DUS3L, PUS1), we observed similar, albeit weaker shifts after 12 h in the respective other metabolite (Figure 2B). This possibly reflects that within the 12 h time frame, the 5-FU metabolites are interconverted between the two sugar forms (deoxyribose and ribose), a process we term "ribose shuffling" (Figure 2C). However, we did not see this effect in all the shifting proteins (e.g., TK1, SAMHD1). It is surprising that FUR already leads to TYMS stabilization after 2 h, when TYMS is expected to be specifically inhibited by the deoxy-metabolite FdUMP. In a lysate WB-CETSA experiment we observed a very clear difference between FdUMP and FUMP's affinity to TYMS (Figure S2B). This suggests that the cellular effects of FUR on TYMS after 2 h might instead be explained by a rapid ribose shuffling that provides sufficient amounts of FdUMP to fully engage TYMS.

In addition to the proteins shifting similarly at 2 h and 12 h, there are other proteins in which we either observed a shift only at 12 h or a much stronger shift at this time point (Figure 2A). These shifts likely reflect downstream events of drug binding including effects on cell-cycle proteins, from which IMPRINTS-CETSA has previously been shown to yield stringent information (Dai et al., 2018). RB1, a key player in the regulation of cell division (Harrington et al., 1998; Knudsen et al., 2000), showed a destabilization for both drugs at 12 h, stronger in FUR, which might indicate hypophosphorylation of RB1 and initiation of S-phase cell-cycle arrest (Dai et al., 2018). A concurrent stabilization of the CDK inhibitor p21 (CDKN1A), also stronger in FUR, could reflect the inhibition of a CDK, attenuating the phosphorylation of RB1. After 12 h of FUR treatment, we also observed very prominent changes in levels of p53-regulated proteins. We observed increased levels of TP53I3, SERPINB5, SFN, and RRM2B, as well as a decrease in ANLN, consistent with p53 activation (Riley et al., 2008). Interestingly these signals were not seen, or were much weaker, in FUDR, although DNA damage repair is assumed to be a key control element for p53 activation (Hafner et al., 2019). We used cells containing a stably integrated, p53-dependent β-galactosidase reporter construct to validate p53 activation (Figure 2D). Cells were treated with the indicated concentrations of FUR or FUDR for 22 h and β-galactosidase intensity was measured. We observed a dose-dependent increase of β-galactosidase signal only for FUR-treated cells reaching similar intensity as compared with the positive control. Additionally, we treated MCF7 cells for 2 h and 12 h with 100 μM FUR, FUDR, or 5-FU and measured levels for p53, as well as downstream p21 and MDM2, with WB (Figure S3). We observed increased levels of p53 after 2 h in FUR-treated and (albeit weaker) in 5-FU-treated, but not in FUDR-treated

(E) ClueGO analysis of hits generated in 5-FU (green), FUDR (blue), and FUR (orange) experiments. Each node represents an enriched GO term. The percentage of contributing hits from each condition is visualized by the amount of color per node (e.g., 100% contribution = single color). Edges between nodes represent relation of GO terms. Left panel compares 5-FU with 2 h FUDR/FUR hits: early FUDR/FUR response. Right panel compares 5-FU with 12 h FUDR/FUR hits: advanced FUDR/FUR response.

cells. Similarly, at 12 h a strongly increased expression of p21 and MDM2 was measured for FUR and a weaker increase for 5-FU. At this time point, FUDR showed a slight increase in p53 levels, but not for p21 or MDM2. This is consistent with the earlier proposed effect of "ribose shuffling" whereby p53 activation in these cells was induced by FUR treatment.

CETSA response to 5-FU is dominated by RNA pathways

As 5-FU compounds are most commonly used in colon cancer therapy, we also performed IMPRINTS-CETSA experiments with 5-FU in the colon cancer cell line HCT15. Due to the slow activation of 5-FU, as judged from previous CETSA studies of direct target engagement with TYMS (Almqvist et al., 2016), the cells were treated with 100 μM 5-FU for 12 h. A comprehensive GO analysis of the 5-FU hits compared with early (2 h) and advanced (12 h) FUDR/FUR hits is summarized in Figure 2E. Part of the responses for the metabolites FUDR and FUR at 2 h formed a significant fraction of the 5-FU response. GO terms related to RNA-modifications were dominated by FUR hits, while terms involving nucleotide metabolism and DNA repair mainly consist of FUDR hits. In contrast, when comparing with the later time point (12 h) the two distinct responses were more evenly balanced, reflecting the earlier-described effect of ribose shuffling between FUR and FUDR. Figure 3A (left panel and small insets) shows the shifting proteins in parental HCT15 cells after 5-FU treatment (referred to as HCT15_Par_5FU) characteristic for and also representing FUR and FUDR responses. Several 5xU-modifying proteins that are stabilized in FUR treatment (PUS1, PUS7, RPUSD1, RPUSD2, TRUB1), as well as additional members such as PUS7L and PUS10, were also stabilized after 5-FU treatment. Similarly, DUS3L and DUS1L showed thermal stabilization. Several methyltransferases including TRMT2A, TRMT10C, THUMPD3, CMTR1, as well as SSB showed comparable IMPRINTS profiles (Figure 3A).

When comparing the 5-FU response with FUDR, proteins in DNA repair and pyrimidine pathways shift similarly. We observed a stabilization for HCMES, FANCI, and FANCD2, which supports comparable DNA damage/repair effects on these proteins after 5-FU and FUDR treatment. The shifts in the pyrimidine pathway proteins include SAMHD1, TK1, DTYMK, and DUT (albeit the last three showed relatively high standard error of the mean (SEM)). Together, the data on these proteins support a similar depletion of thymidine nucleotides and buildup of dUMP/dUTP after treatment with the two drugs.

In addition to proteins previously responding in the FUR or FUDR datasets, several other protein clusters were seen to respond only in the 5-FU data. One prominent example of unique 5-FU hits is a subset of tRNA ligases (Figure S4A) including EPRS, IARS, RARS, and LARS. Three additional members show similar shifts, albeit with either a weaker intensity (QARS and YARS) or higher variation (MARS). Together with the aminoacyl tRNA synthase complex-interacting scaffolding subunits AIMP1, AIMP2, and AIMP3, they constitute most of the components of the multi-tRNA synthetase complex (MSC) (Figure S4B) (Han et al., 2003). These proteins showed similar IMPRINTS profiles as well as melt curves (Figure S4C) and likely shift as a complex, which has been previously observed with IMPRINTS-CETSA during S-phase progression of the cell cycle (Dai et al., 2018).

Deconvoluting critical efficacy components in a 5-FU resistance model

To study the effects of the observed 5-FU CETSA responses on a resistant cell model, we then went on to collect data from 5-FU-resistant HCT15 cells. Resistance to 5-FU was established *in vitro* so that cells reached a similar growth rate in the presence of 16 μM and 100 μM 5-FU as compared with their untreated parental counterparts (Figure S5A). A cell-viability assay at 4 days with increasing doses of 5-FU demonstrated an increase of about two orders of magnitude in effective 5-FU concentration in the case of resistant HCT15 cells (Figure S5B). In an initial experiment, as illustrated in Figure 3B, we assessed whether the 5-FU hits in parental HCT15 treated with 100 μM 5-FU (referred to as HCT15_Par_5FU) were similarly affected by 5-FU in the resistant cells that were maintained at 16 μM 5-FU (referred to as HCT15_Res_5FU). Additionally, we collected a dataset comparing resistant HCT15 cells treated with 16 μM and 100 μM 5-FU (referred to as HCT15_Res_Diff) to monitor the differential effects in these cells. These results confirm that only a small number of proteins, mostly involved in metabolic pathways (some discussed below), were differentially shifted due to the increased 5-FU concentration. Together, these experiments allowed us to monitor how resistance affects each CETSA shift in the complex response of 5-FU discussed above, and therefore to prioritize which of these individual responses may be essential for the 5-FU MoA.

In some proteins and pathways, the responses in parental cells are maintained in resistant HCT15 cells. We concluded that these were non-essential responses for cytotoxicity and in the MoA of 5-FU. Surprisingly, the CETSA response for the anticipated major protein target, TYMS, was equally affected in parental and resistant cells, where an increased 5-FU concentration had no further effect on protein stability (Figure 3C). Interestingly, TYMS response was saturated at both these concentrations (Figure S5C) and was likely fully inhibited under these conditions in resistant cells. There were also responses involved in other cellular processes, e.g., mitochondrial respiration (UQCRC2, ATP5F1A, SDHAF2) or metabolic pathways (ETNK1, SRM, OAT) that were not attenuated in resistant cells, suggesting that they were non-essential for drug toxicity (Figure S5D). In other proteins and pathways, however, the responses observed in parental HCT15 cells were attenuated, supporting the existence of evolutionary pressure to diminish these specific responses in order to allow cell proliferation. The most notable attenuation effects involved proteins in RNA-modifications and interactions (Figure 3A, middle panel and small insets). These included the 5xU-modifying proteins, initially identified in response to FUR treatment, such as Ψ-synthases where the prominent responses of PUS7L, PUS10, and RPUSD1 in parental cells were attenuated in resistant HCT15 cells, while the responses for other PUS family members were completely diminished. A similar IMPRINTS profile was observed for TRMT2A, where the response was only a fraction of that of parental cells. The stabilizations of DUS1L and DUS3L as well as tRNA MSC subunits were also completely attenuated. Responses in RNA-interacting proteins involved in ribosomal biogenesis and ribosomal subunit export were also abrogated, out of which MRTO4, NLE1, and BYSL were observed as hits in FUR while several others, e.g., NUP88, PELP1, RIOK3,

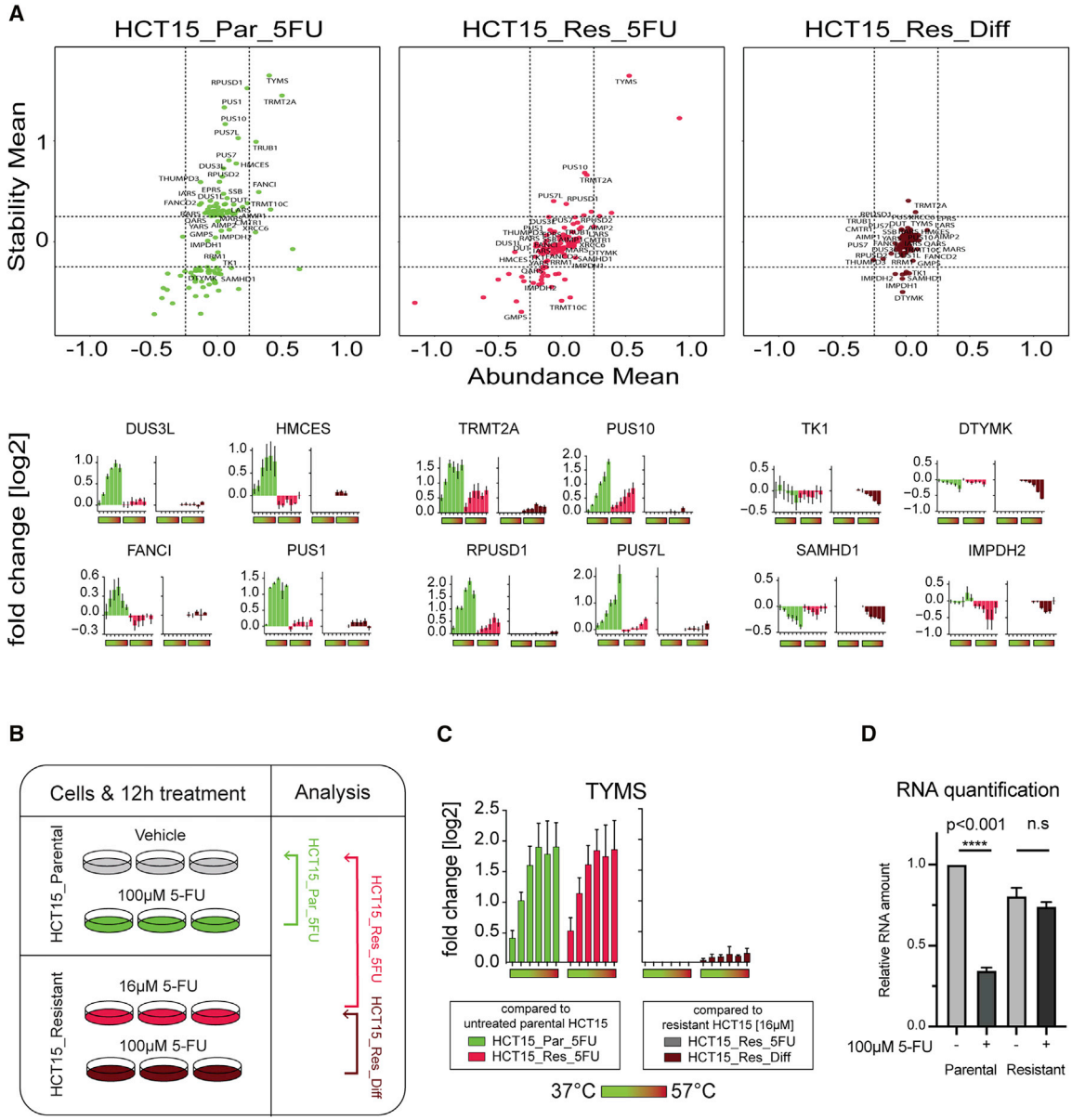

Figure 3. Deconvoluting critical efficacy components in a 5-FU resistance model

(A) Scatterplots of protein mean abundance changes versus mean thermal stability changes (STAR Methods) for proteins with changed PRINTS identified in the HCT15_Par_5FU analysis (left panel) and the corresponding ones in HCT15_Res_5FU (middle panel) and HCT15_Res_Diff (right panel). IMPRINTS profiles of selected proteins are shown in the small insets below and presented as mean log2 fold change compared to the reference ±SEM from biological replicates (n = 3).

(B) Treatment conditions for IMPRINTS-CETSA using parental and resistant HCT15 cells. Parental cells were treated for 12 h with either vehicle (gray) or 100 μM 5-FU (green), while resistant cells were treated with either 16 μM 5-FU (red) or 100 μM 5-FU (brown). Two conditions were compared with each other, resulting in three types of analysis indicated by colored arrows.

(C) IMPRINTS profiles of TYMS for the different types of analysis. Data are presented as mean $\log_2$ fold change compared to the reference ±SEM from biological replicates (n = 3).

(D) RNA quantification in parental versus resistant cells after 12 h of treatment with 100 μM 5-FU or vehicle. Data are normalized to parental vehicle treatment and represent two biological replicates with two technical replicates each. Unpaired t tests for vehicle and 5-FU treatment are shown, respectively.

RSL24D1, SDAD1, and AMD1, were not measured in the FUR/FUDR datasets (Figure S5E). To shed light on potential global effects on RNA synthesis and stability, we further quantified RNA levels in parental as well as resistant cells after 12 h of 100 μM 5-FU or vehicle treatment (Figure 3D). To encompass tRNAs and other small RNAs, e.g., small nuclear RNA and snoRNA, we used a total transcriptome isolation protocol (described in method details). A significant decrease in RNA levels was observed in parental cells after 5-FU treatment, while the levels were not significantly affected in resistant cells.

While the strongest responses in FUR are attenuated, similar analysis of FUDR hits showed that key proteins in this pathway

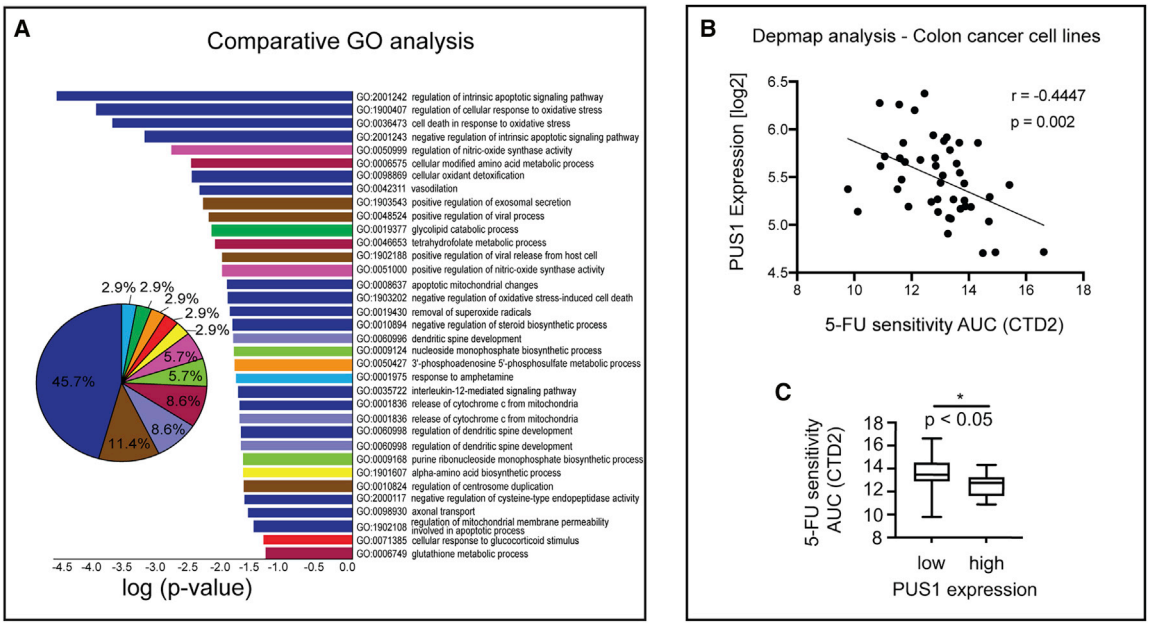

Figure 4. Differentially expressed proteins in resistant HCT15 cells

(A) Comparative GO analysis of hits with expression changes in HCT15_Res_5FU. Each bar represents one enriched GO (biological processes) term; the size of the bar represents the log(p value). Colors of bars represent different clusters, and the percentage of each cluster affected among all GO terms is reflected in the pie chart.

(B) Depmap Pearson correlation analysis between 5-FU sensitivity and PUS1 expression in colon cancer cell lines (n = 45)

(C) 5-FU sensitivity in PUS1-low- versus -high-expressing colon cancer cell lines (n = 45). Data are presented as box plots and the p value was calculated by performing an unpaired two-tailed t test.

(including TK1, DTYMK, and IMPDH2) were affected but did not reach our hit selection criteria in parental cells due to high SEM in these measurements. However, the overall impression is that the responses in DNA repair proteins (HMCES, FANCD2, FANCI) and several thymidine-sensitive proteins (e.g., SAMHD1) are diminished.

As mentioned above, the comparison of resistant HCT15 cells treated with 16 μM and 100 μM 5-FU (Figure 3A, right panel and small insets) revealed identical IMPRINTS-CETSA profiles for nearly all proteins. Among the few hits, proteins in the thymidine metabolism pathway (SAMHD1, TK1, DTYMK) as well as purine response (IMPDH1, IMPDH2) were affected by the higher 5-FU concentration. Together, this supports a scenario whereby the provision of nucleotides is still limited by 5-FU in resistant cells, but this is not the most critical component of the 5-FU toxicity in this model.

In addition to the stability changes in the resistant cells (compared with the parental cells), we observed many proteins with expression changes. Comprehensive changes of the levels of many proteins in drug-resistant cells have previously been observed using quantitative proteomics (Cree and Charlton, 2017). Many of these changes represent modulation of cellular programs counteracting general cytotoxic effects. Notable protein-level changes comprise increased expression of proteins in oxidative stress responses (typically regulated by NRF2), apoptosis, nucleoside metabolic pathways, and regulation of mitotic cycle (Figure 4A). These responses are very complex and likely involve activation of general fitness and stress pathways, typically also affected by other drugs with different chemical structures and MoAs (Sun et al., 2019). The specific contribution to the 5-FU resistance in this model, however, is best illustrated by the attenuation of the parental CETSA signals as discussed above. We propose that these reduced CETSA signals in resistant cells are due to the refined modulation of the pool sizes of all the different (fluoro-)uridine-based metabolites (U-pools, as discussed below), whereby a subtle balance is required to provide sufficient uridine nucleotides to promote cell growth while at the same time attenuating toxic fluorouridine nucleotide pools. We note that one strongly modulated protein with decreased levels in resistant cells is UMP synthase (UMPS) constituting one path for 5-FU activation (Figure S6). Downregulation of UMPS may compromise 5-FU activation that leads to RNA cytotoxicity, thus contributing to a decreased incorporation of FUTP into RNA.

To shed further light on the mechanism of resistance and the effects of variations in U-pools, we treated resistant HCT15 cells with the 5-FU metabolites FUR and FUDR for 48 h. We observed partly increased sensitivity with both metabolites as compared with 5-FU in resistant cells (Figure S5F). This could be explained by both compounds bypassing a resistance mechanism involving the attenuated expression of UMPS, but might also be due to a slower activation of 5-FU compared with FUR and FUDR (Almqvist et al., 2016). Interestingly, while FUDR has the same activity in resistant and parental cells, FUR is significantly less active in the resistant cells and therefore behaves similarly to 5-FU. This further supports that the resistance mechanism primarily attenuates RNA-related toxicity.

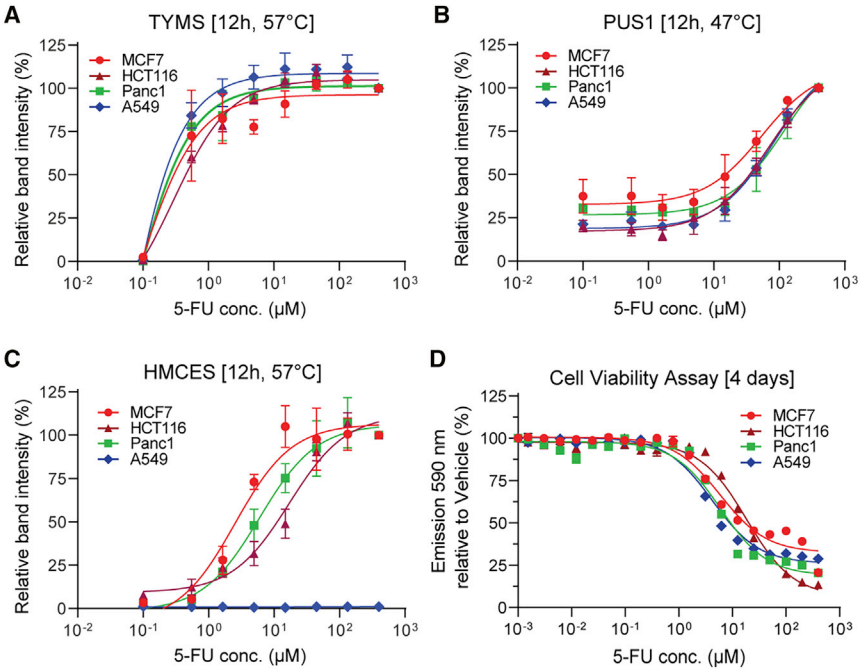

Figure 5. $ITDR_{CETSA}$ responses as candidate biomarkers for 5-FU in different cell lines

(A–C) MCF7 (red), HCT116 (brown), Panc-1 (green), and A549 (blue) cells were treated with increasing concentrations of 5-FU for 12 h. WB analyses of TYMS, PUS1, and HMCES were performed for each cell line. A dose-dependent stabilization was observed for all tested cell lines for (A) TYMS at 57°C and (B) PUS1 at 47°C. Comparable stabilization can be seen in three out of four cell lines for (C) HMCES at 57°C.

(D) Cell viability assays at 4 days of incubation with increasing 5-FU concentrations show similar curves for all tested cell lines.

All data represent the mean ± SEM from biological replicates (n = 3).

Additionally, we explored the "Cancer Dependency Map" (Depmap) database that systematically identifies genetic and pharmacological dependencies and biomarkers. We analyzed PUS1 expression in colon cancer cell lines (n = 45) and observed a negative correlation between PUS1 expression and 5-FU sensitivity (Figure 4B). Similarly, when dividing the cell lines into PUS1-low- and PUS1-high-expressing cells, we found a significant difference in their 5-FU sensitivity (Figure 4C). Together, these results are consistent with putative PUS1-(5-FU) RNA inhibitory complexes specifically contributing to toxicity, which is partly abrogated by lower expression of PUS1.

CETSA responses as candidate mechanistic biomarkers for 5-FU efficacy

Based on the studies above, we propose that a small set of the CETSA-responsive proteins could serve as early candidate mechanistic biomarkers for 5-FU efficacy. We therefore selected representative proteins for RNA-processing (PUS1), pyrimidine metabolism (TYMS), and DNA repair (HMCES), and verified their CETSA responses in four cell lines (MCF7, breast adenocarcinoma; Panc-1, pancreatic carcinoma; HCT116, colorectal carcinoma; and A549, pulmonary adenocarcinoma) to investigate the generality of these effects in different cancer cell types (Figures 5A–5C). A dose-dependent stabilization of TYMS and PUS1 could be observed in all tested cell lines, while HMCES gave a response in three cell lines, with no stabilization in A549 cells. In parallel, we performed viability assays in these cell lines showing similar sensitivity to 5-FU (Figure 5D). The demonstrated PUS1 response appears to be a requirement for cytotoxicity, and thus this protein could now serve as a candidate efficacy biomarker for the "RNA axis" in 5-FU MoA.

To test whether the 5-FU response could be replicated in animals, we used a mouse MCF7 xenograft model to collect an MS-$ITDR_{CETSA}$ dataset (Figure 6A). The mice were sacrificed after 22 h of 5-FU exposure, tumor pieces were heated at 37°C or 52°C, and MS data were collected and analyzed. In parallel, CETSA melting curves for TYMS were generated using AlphaLISA detection, demonstrating a clear stabilization of TYMS in the mice xenografts (Figure 6B). In the MS-$ITDR_{CETSA}$ data, in addition to TYMS, stabilizations were seen for several 5xU-modifying proteins (Figures 6C and 6D). These include TYMS, PUS10, TRUB1, PUS7, PUS1, and TRMT2A, the latter three being among the stronger shifting proteins in 5-FU-treated HCT15 cells. These data support that interaction changes within these proteins can be measured in animal tissues during drug treatment and therefore could also potentially serve as candidate biomarkers for 5-FU efficacy in human tumor biopsies (Langebäck et al., 2019).

DISCUSSION

Antimetabolite-based cancer drugs in clinical use typically have complex MoAs that are often only partially understood. MoAs involving polypharmacology are likely a common feature of effective antimetabolites: by acting on multiple pathways/targets, drug resistance is less likely. More detailed insights into the MoAs of antimetabolites in clinical use can therefore help in establishing mechanistic-efficacy biomarkers and aid in defining optimal combination therapies to minimize drug resistance. Furthermore, a better overview of "the space of cancer drug targets," as provided by detailed mechanistic information, also contributes specific candidates for the development of cancer drugs with new properties.

In the present study, we apply the novel high-resolution IMPRINTS-CETSA technique to analyze the MoA of the antimetabolite 5-FU and its metabolites FUR and FUDR. 5-FU has been extensively studied for more than 60 years during which some principal components of its MoA have been put forward including TYMS inhibition, modulation of metabolic and signaling pathways, DNA damage and repair, and incorporation of 5-FU into RNA (Vodenkova et al., 2020). Eventually the ensemble of MoA components leads to p53 activation, cell-cycle arrest,

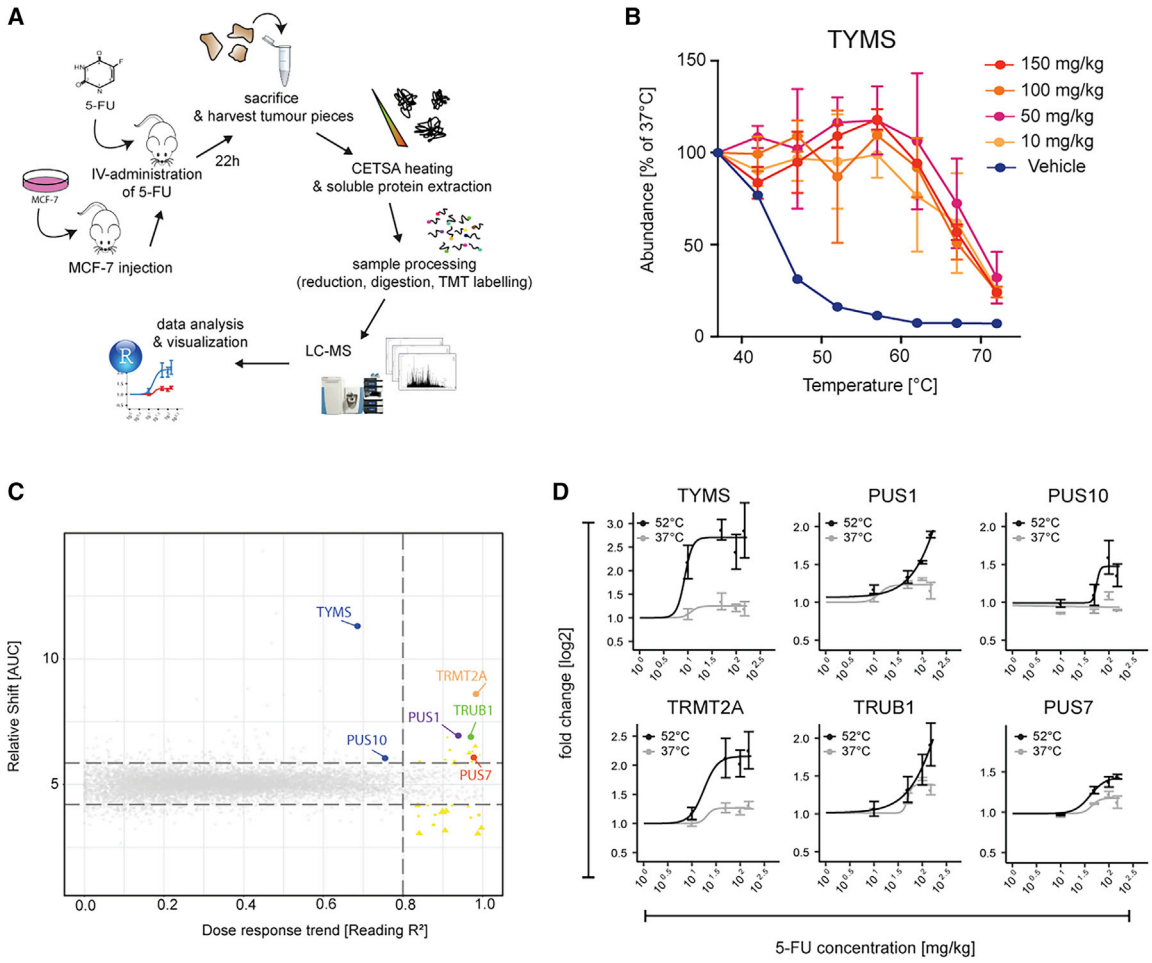

Figure 6. CETSA responses as candidate biomarkers for 5-FU: clinical mouse model

(A) Experimental design of mouse xenograft experiment. MCF7 cells were injected into mice. After 22 h of 5-FU treatment the tumors were harvested and analyzed (see method details).

(B) CETSA melt curves with AlphaLISA show the melting profiles for TYMS in tumor pieces. Treatment conditions are visualized by different colors: vehicle, dark blue; 10 mg/kg, yellow; 50 mg/kg, magenta; 100 mg/kg, orange; 150 mg/kg, red. Data are presented as percent of 37°C ± SEM.

(C) Scatterplot visualizes proteins with thermal stabilization in the LC-MS dataset (STAR Methods). Proteins of interest are labeled. Unresponsive proteins are depicted in gray.

(D) $ITDR_{CETSA}$ profiles of TYMS, TRMT2A, PUS1, PUS10, TRUB1, and PUS7 in tumor pieces analyzed with LC-MS. Data are presented as mean fold change ±SEM compared to vehicle from technical replicates.

and/or apoptosis. However, despite the vast amount of information available, a conclusive and systems-wide understanding of 5-FU MoA has been elusive, the molecular mechanisms of its DNA- and RNA-mediated toxicity have been poorly defined, and, partly due to this, stringent biomarkers to guide 5-FU therapy are missing. Here we establish a range of changes in PRINTS, whereby each protein or ensemble reports on a specific aspect of the 5-FU MoA. Although some of the identified proteins are known or anticipated players, most constitute novel potential components of the 5-FU MoA.

Prominent CETSA effects were seen for proteins performing RNA-modifications or involved in ribosome biogenesis and mRNA processing. Two Ψ-synthases have previously been identified as candidates for 5-FU MoA in non-mammalian cells (*C. elegans* and oocytes) (Zhao and Yu, 2007), but here we identify six family members as likely targets for 5-FU-modified RNAs in human cells. Four RNA methylases were also identified, out of which only one was previously implicated in 5-FU MoA (Tseng et al., 1978). In addition, two dihydrouridine synthases, members of a family previously not associated with the 5-FU MoA, are involved. It is likely that for most of these 5xU-modifying enzymes, the CETSA shifts represent specific, often covalent, inhibitory interactions with 5-FU-modified RNA. tRNAs, but also rRNAs, mRNAs, and snoRNAs can serve as substrates for RNA-modifying enzymes. Based on the present data (and analysis of the related literature), we cannot conclude which of these substrates represent the most important downstream effects of the 5-FU MoA. However, we show an inverse correlation of PUS1 expression to 5-FU sensitivity in a set of 45 cell lines, consistent with a role of PUS1 in the toxicity of 5-FU. The shift in the tRNA MSC might reflect an altered binding to differentially modified tRNAs. Also, shifts in RNA-processing proteins, not directly

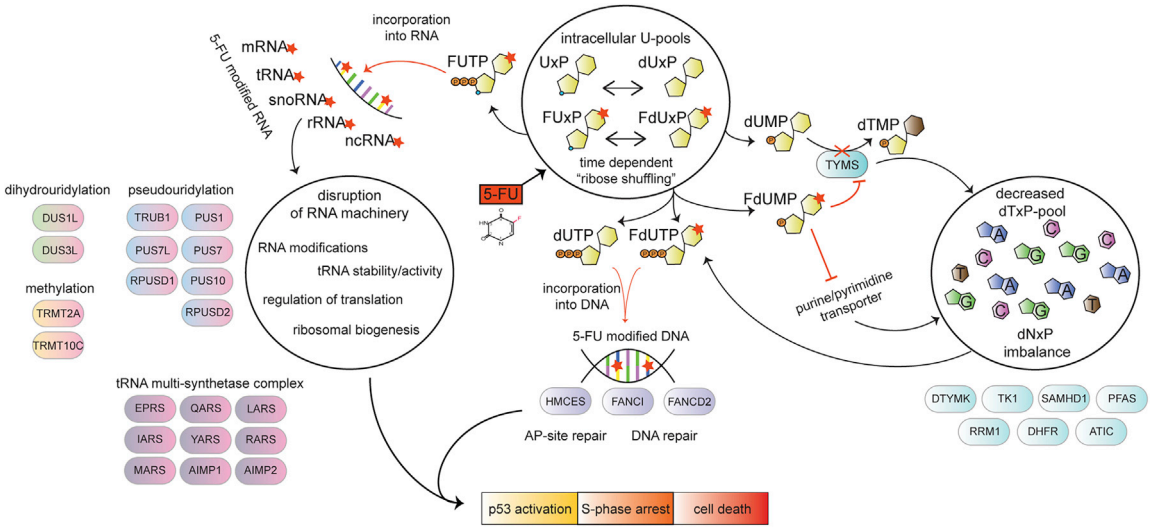

Figure 7. Schematic illustration of proposed 5-FU MoA and biomarkers for response

5-FU enters the cell and affects intracellular uracil-pools (U-pools). Active metabolites of 5-FU affect several cellular pathways including dTxP-pool, DNA repair, and the RNA machinery. Direct effects of the active 5-FU metabolites (FdUMP, FUTP, and FdUTP) are shown in red. Proteins identified in this study that reflect 5-FU response in different cellular pathways are shown in different colors: light blue, proteins affecting dNTP imbalance; purple, proteins involved in DNA repair; magenta, proteins affecting the RNA machinery. Other reactions and consequences depicted here (e.g., p53 activation, S-phase arrest, and cell death) represent downstream effects.

involved in catalyzing modifications but, for example, in ribosomal biogenesis, might be due to altered modifications of rRNA. Strong support for the critical importance of interactions with 5-FU-modified RNA for 5-FU cytotoxic effect comes from the prominent attenuation of these signals in resistant HCT15 cells, while other responses, e.g., proteins in metabolism and mitochondrial respiration, are not attenuated. Additionally, the decrease in RNA levels after 5-FU treatment in parental cells but not in resistant cells further strengthens the importance of RNA-mediated cytotoxicity. Another indication for the crucial effect of 5-FU on the cellular RNA machinery is the downregulation of UMPS in resistant cells. This disrupts the direct metabolism of 5-FU into FUMP and therefore the incorporation into RNA and its subsequent effects. This might be a contributing factor to why FUR and FUDR have some activity in 5-FU-resistant cells. Despite being one of the most used cancer drugs, the revelation that 5-FU acts dominantly on RNA-modifying processes supports that such pathways might be underexplored as cancer drug targets.

Our data also support that levels of proteins under the transcriptional control of p53 activation are important downstream signals of the RNA-induced toxicity in 5-FU-sensitive MCF7 cells. Interestingly, such changes are much less pronounced in FUDR, in contrast to the expectation that 5-FU-induced DNA damage is the key activator of p53 (Hafner et al., 2019). Note that we do not observe a p53 response in HCT15 cells, which is consistent with the p53 deficiency in this cell line (Adamsen et al., 2011). Although 5-FU modified RNA has been previously implicated in the 5-FU MoA, it is most often considered as an additional element on top of the core components, i.e., distortion of the deoxypyrimidine metabolism and DNA damage. Together, our data support that 5-FU-modified RNA might be the central component of the 5-FU MoA, at least in the studied systems.

We also identified DNA repair proteins such as HMCES and the FANCD2/FANCI complex to be involved in the 5-FU MoA. The observed HMCES stabilization indicates a protein-DNA interaction following the excision of (fluoro-)uracil nucleobases from DNA, in agreement with recent findings whereby HMCES has emerged as a key protein in AP-site repair by forming a covalent interaction with ssDNA.

A surprising observation is that 5-FU-resistant cells proliferate in the presence of 5-FU while TYMS is inhibited. This is intriguing considering the critical role expected from TYMS inhibition in the 5-FU MoA. 5-FU does not have prominent effects on thymidine nucleotide levels, as judged from the small shifts of the thymidine-sensitive ensemble (TK1, DTYMK, and RRM1) in parental cells. In the resistant cells, however, at higher 5-FU concentration these proteins still give distinct shifts, as do other FUDR-sensitive proteins in the purine metabolism, suggesting that thymidine levels are not the most critical component of the 5-FU MoA. Furthermore, decreases in deoxythymidine triphosphate levels have been found to be well tolerated in yeast and led to mild or no cell-growth defects, which further supports our findings (Sánchez et al., 2012). Our data instead point to a buildup of intracellular (fluoro-)uridine nucleotide pools as judged from the DUT stabilization. However, a scenario in which some thymidine is provided from the cell-culture media is possible and, as a result, the decrease in thymidine levels induced by TYMS inhibition is not limiting for cell growth.

In the discussion above we focus on the likely core components of 5-FU MoA, as summarized in Figure 7. A key focus in previous studies of 5-FU response and resistance has been to correlate levels (protein or mRNA) of TYMS and other enzymes involved in 5-FU activation (e.g., UMPS, UCK1/2, UPP1/2, PPAT) and catabolism (in particular dihydropyrimidine dehydrogenase) to cellular or clinical efficacy (Iacovides et al., 2018;

Marin-Vicente et al., 2013; Rodrigues et al., 2019; Tieng et al., 2020). Although some correlations have been found, analyses based only on levels have not yet yielded robust clinical biomarkers. Since the most prominent proteome modulations we report in this study are likely sensitive to U-pool levels, we hypothesize that the relative sizes of all the different pools of uridine and fluorouridine nucleotides are key determinants of 5-FU toxicity. However, the regulation of such pool sizes is very complex and involves the intrinsic activity of enzymes controlling both uridine and fluorouridine pools, which in turn depends on the genetic background, enzyme levels, and activation states of enzymes in the studied cells. Pool sizes also depend on the extracellular provision of (fluoro-)uridine bases and nucleotides, determined by the cell/tumor context and transport processes. During resistance development, cells have to balance the attenuation of fluorouracil-containing metabolites against the requirement of sufficient levels of physiological uracil-containing metabolites. Direct measurements of some of the U-pools in cells and tumor samples have been attempted but have not yielded robust biomarkers—stringent measurements of ensembles of metabolites in clinical samples are in general very challenging (Derissen et al., 2015, 2016).

The CETSA shifts discovered in the present work constitute interesting alternative 5-FU efficacy biomarkers, as they capture the direct effects of the U-pools on the proteome, including a multitude of downstream effects of the incorporation of these pools into RNA and DNA. An enabling factor is the robustness of the CETSA experiment due to the key measurement step—heating—being performed in intact cells, and the sensitivity of the IMPRINTS-CETSA method. Furthermore, CETSA experiments at early time points are highly informative and translatable, which is illustrated by the similarity of shifts of individual proteins observed for FUR and FUDR in MCF7 breast cancer cells compared with shifts for 5-FU in HCT15 colon cancer cells, as well as the reproducibility of key shifts in a diverse set of cell lines and xenograft tissues. Several of these mechanistic biomarkers can now serve as minimal determinants for 5-FU activity and be tested in clinical studies as an initial filter for patient selection. It can be noted that resistance downstream of the observed effects might still develop and attenuate drug activity by, for example, altering p53 signaling or apoptosis response, whereby additional complementary biomarkers could be investigated. In the present work, we also confirm that IMPRINTS-CETSA is a highly sensitive method for studies of PRINTS and can provide novel critical information on the MoA, even for very well-studied clinical drugs. Therefore, the applied strategy whereby several similar cancer drugs are studied in parallel at multiple time points, including resistance models, could be valuable in teaching us the tricks of many other cancer drugs in clinical use.

SIGNIFICANCE

Our current understanding of the mechanism of action (MoA) of many cancer drugs is still incomplete. This hampers, for example, efforts in establishing efficient personalized medicine regimens, the optimization of combination therapies, and the development of next-generation drugs. In the present work we explore IMPRINTS-CETSA, a stringent interaction proteomics method, in the study of cancer drug action, specifically the MoA of 5-fluorouracil (5-FU)-based drugs. We focus on the relatively early drug effects, up to 12 h, when this time frame is less accessible to other omics methods while critical for defining drug MoAs. Using this approach, we discovered a battery of proteins that are affected, where some are likely to be direct drug targets of 5-FU-modified RNA or DNA. Most of these proteins have not previously been assigned as 5-FU drug targets or implicated in the MoA of 5-FU. We also provide support that the previously major protein target, TYMS, might not be as important in the 5-FU MoA as anticipated. While 5-FU is one of the most used and studied cancer drugs, this novel information significantly expands our understanding of the 5-FU MoA and will be important to direct further work toward dissecting its complete MoA. Furthermore, the CETSA responses of several proteins now provide ideal readouts for directly monitoring whether the required 5-FU effects are accomplished in specific patient or tissue contexts. Therefore, some of the proteins highlighted in this study are CETSA-based candidate biomarkers that can now be examined in clinical studies. Together, this work validates a novel strategy to dissect the MoA of cancer drugs, which could be broadly applicable to other cancer drugs in clinical use or in development.

STAR★METHODS

Detailed methods are provided in the online version of this paper and include the following:

- KEY RESOURCE TABLE
- RESOURCE AVAILABILITY
  - Lead contact
  - Materials availability
  - Data and code availability
- EXPERIMENTAL MODEL AND SUBJECT DETAILS
  - Cell lines
  - Mouse models
- METHOD DETAILS
  - The cellular thermal shift assay (CETSA)
  - Cell proliferation and viability assays
  - AlphaLISA
  - p53-activation reporter assay
  - RNA isolation and quantification
  - Western blot
  - Sample preparation for LC-MS
  - LC-MS
- QUANTIFICATION AND STATISTICAL ANALYSIS
  - Protein identification and quantification
  - Quantitative MS data analysis and visualisation
  - Protein-protein interaction network and gene ontology (GO) enrichment analysis
  - Analysis and visualisation of melt curve MS-CETSA, $ITDR_{CETSA}$, and cell viability data
  - Correlation analysis

SUPPLEMENTAL INFORMATION

Supplemental information can be found online at https://doi.org/10.1016/j.chembiol.2021.06.007.

ACKNOWLEDGMENTS

We thank all past and current members of the Nordlund laboratory at Nanyang Technological University, A*STAR, and Karolinska Institutet, who have contributed to the development of CETSA. We also thank Sophia Ceder for discussion and advice on experimental design and data analysis. We gratefully acknowledge funding from a start-up grant from Nanyang Technological University and grants from the Swedish Research Council, the Swedish Cancer Society, Radiumhemmets funds, and the Knut and Alice Wallenberg Foundation, as well as Kent Cancer Trust, Frankfurter Stiftung für krebskranke Kinder and Hilfe für krebskranke Kinder Frankfurt. This work is also supported by the Singapore's National Research Foundation (NRF-CRP22-2019-0003) awarded to N.P., P.N.. and L.D.

AUTHOR CONTRIBUTIONS

Conceptualization, P.N.; methodology, Y.Y.L., S.B., L.S., L.D., T.S., Y.C., N.P., M.M., J.C., C.R.C., D.P.L., and P.N.; formal analysis, Y.Y.L., A.D.R., S.B., L.D., and P.N.; investigation, Y.Y.L., S.B., L.S., and A.D.R.; writing – original draft, P.N., Y.Y.L., and S.B.; writing – review & editing, all authors; funding acquisition, P.N. and N.P.; supervision, P.N.

DECLARATION OF INTERESTS

P.N. is the inventor of patents related to the CETSA method and is a cofounder and board member of Pelago Biosciences AB. No other authors have competing interests.

Received: March 31, 2021
Revised: May 14, 2021
Accepted: June 25, 2021
Published: July 14, 2021

REFERENCES

Adamsen, B.L., Kravik, K.L., and De Angelis, P.M. (2011). DNA damage signaling in response to 5-fluorouracil in three colorectal cancer cell lines with different mismatch repair and TP53 status. Int. J. Oncol. *39*, 673–682.

Almqvist, H., Axelsson, H., Jafari, R., Dan, C., Mateus, A., Haraldsson, M., Larsson, A., Molina, D.M., Artursson, P., Lundbäck, T., et al. (2016). CETSA screening identifies known and novel thymidylate synthase inhibitors and slow intracellular activation of 5-fluorouracil. Nat. Commun. *7*, 11040.

Caradonna, S.J., and Cheng, Y.C. (1980). The role of deoxyuridine triphosphate nucleotidohydrolase, uracil-DNA glycosylase, and DNA polymerase α in the metabolism of FUdR in human tumor cells. Mol. Pharmacol. *18*, 513–520.

Carter, J.M., Emmett, W., Mozos, I.R., Kotter, A., Helm, M., Ule, J., and Hussain, S. (2019). FICC-Seq: a method for enzyme-specified profiling of methyl-5-uridine in cellular RNA. Nucleic Acids Res. *47*, e113.

Chang, Y.H., Nishimura, S., Oishi, H., Kelly, V.P., Kuno, A., and Takahashi, S. (2019). TRMT2A is a novel cell cycle regulator that suppresses cell proliferation. Biochem. Biophys. Res. Commun. *508*, 410–415.

Christensen, S., Van der Roest, B., Besselink, N., Janssen, R., Boymans, S., Martens, J.W.M., Yaspo, M.L., Priestley, P., Kuijk, E., Cuppen, E., et al. (2019). 5-Fluorouracil treatment induces characteristic T>G mutations in human cancer. Nat. Commun. *10*, 4571.

Cree, I.A., and Charlton, P. (2017). Molecular chess? Hallmarks of anti-cancer drug resistance. BMC Cancer *17*, 10.

Cronstein, B.N., and Aune, T.M. (2020). Methotrexate and its mechanisms of action in inflammatory arthritis. Nat. Rev. Rheumatol. *16*, 145–154.

Dai, L., Zhao, T., Bisteau, X., Sun, W., Prabhu, N., Lim, Y.T., Sobota, R.M., Kaldis, P., and Nordlund, P. (2018). Modulation of protein-interaction states through the cell cycle. Cell *173*, 1481–1494 e13.

Dai, L., Prabhu, N., Yu, L.Y., Bacanu, S., Ramos, A.D., and Nordlund, P. (2019). Horizontal cell Biology: monitoring global changes of protein interaction states with the proteome-wide cellular thermal shift assay (CETSA). Annu. Rev. Biochem. *88*, 383–408.

Van Der Jeught, K., Xu, H.C., Li, Y.J., Lu, X. Bin, and Ji, G. (2018). Drug resistance and new therapies in colorectal cancer. World J. Gastroenterol. *24*, 3834–3848.

Derissen, E.J.B., Hillebrand, M.J.X., Rosing, H., Schellens, J.H.M., and Beijnen, J.H. (2015). Development of an LC-MS/MS assay for the quantitative determination of the intracellular 5-fluorouracil nucleotides responsible for the anticancer effect of 5-fluorouracil. J. Pharm. Biomed. Anal. *110*, 58–66.

Derissen, E.J.B., Jacobs, B.A.W., Huitema, A.D.R., Rosing, H., Schellens, J.H.M., and Beijnen, J.H. (2016). Exploring the intracellular pharmacokinetics of the 5-fluorouracil nucleotides during capecitabine treatment. Br. J. Clin. Pharmacol. *81*, 949–957.

Deveci, H.A., Nazıroğlu, M., and Nur, G. (2018). 5-Fluorouracil-induced mitochondrial oxidative cytotoxicity and apoptosis are increased in MCF-7 human breast cancer cells by TRPV1 channel activation but not *Hypericum perforatum* treatment. Mol. Cell. Biochem. *439*, 189–198.

Dziekan, J.M., Wirjanata, G., Dai, L., Go, K.D., Yu, H., Lim, Y.T., Chen, L., Wang, L.C., Puspita, B., Prabhu, N., et al. (2020). Cellular thermal shift assay for the identification of drug-target interactions in the *Plasmodium falciparum* proteome. Nat. Protoc. *15*, 1881–1921.

Grem, J.L. (2000). 5-Fluorouracil: forty-plus and still ticking. A review of its preclinical and clinical development. Invest. New Drugs *18*, 299–313.

Gu, X., Liu, Y., and Santi, D.V. (1999). The mechanism of pseudouridine synthase I as deduced from its interaction with 5-fluorouracil-tRNA. Proc. Natl. Acad. Sci. U S A *96*, 14270–14275.

Hafner, A., Bulyk, M.L., Jambhekar, A., and Lahav, G. (2019). The multiple mechanisms that regulate p53 activity and cell fate. Nat. Rev. Mol. Cell Biol. *20*, 199–210.

Halabelian, L., Ravichandran, M., Li, Y., Zeng, H., Rao, A., Arrowsmith, C.H., Consortium, G., Jolla, L., Jolla, L., Jolla, L., et al. (2019). Structural basis of HMCES interactions with abasic DNA and multivalent substrate recognition. Nat. Struct. Mol. Biol. *26*, 607–612.

Han, J.M., Kim, J.Y., and Kim, S. (2003). Molecular network and functional implications of macromolecular tRNA synthetase complex. Biochem. Biophys. Res. Commun. *303*, 985–993.

Harrington, E.A., Bruce, J.L., Harlow, E., and Dyson, N. (1998). pRB plays an essential role in cell cycle arrest induced by DNA damage. Proc. Natl. Acad. Sci. U S A *95*, 11945–11950.

Iacovides, D., Loizides, C., Mitsis, G., and Strati, K. (2018). Whole transcriptome sequence data of 5-FU sensitive and 5-FU resistant tumors generated in a mouse model of de novo carcinogenesis. Data Br. *20*, 1602–1606.

Iyevleva, A.G., Buslov, K.G., Togo, A.V., Matsko, D.E., Filimonenko, V.P., Moiseyenko, V.M., and Imyanitov, E.N. (2007). Measurement of DPD and TS transcripts aimed to predict clinical benefit from fluoropyrimidines: confirmation of the trend in Russian colorectal cancer series and caution regarding the gene referees. Onkologie *30*, 295–300.

Kato, T., Daigo, Y., Hayama, S., Ishikawa, N., Yamabuki, T., Ito, T., Miyamoto, M., Kondo, S., and Nakamura, Y. (2005). A novel human tRNA-dihydrouridine synthase involved in pulmonary carcinogenesis. Cancer Res. *65*, 5638–5646.

Knudsen, K.E., Booth, D., Naderi, S., Sever-Chroneos, Z., Fribourg, A.F., Hunton, I.C., Feramisco, J.R., Wang, J.Y.J., and Knudsen, E.S. (2000). RB-dependent S-phase response to DNA damage. Mol. Cell. Biol. *20*, 7751–7763.

Kotchetkov, R., Driever, P., Cinatl, J., Michaelis, M., Karaskova, J., Blaheta, R., Squire, J., Von Deimling, A., Moog, J., and Cinatl, J. (2005). Increased malignant behavior in neuroblastoma cells with acquired multi-drug resistance does not depend on P-gp expression. Int. J. Oncol. *27*, 1029–1037.

Kuipers, E.J., Grady, W.M., Lieberman, D., Seufferlein, T., Sung, J.J., Boelens, P.G., van de Velde, C.J.H., and Watanabe, T. (2015). Colorectal cancer. Nat. Rev. Dis. Prim. *1*, 15065.

Langebäck, A., Bacanu, S., Laursen, H., Mout, L., Seki, T., Erkens-Schulze, S., Ramos, A.D., Berggren, A., Cao, Y., Hartman, J., et al. (2019). CETSA-based target engagement of taxanes as biomarkers for efficacy and resistance. Sci. Rep. *9*, 19384.

Ledford, H. (2019). Many cancer drugs aim at the wrong molecular targets. Nature. https://doi.org/10.1038/d41586-019-02701-6.

Lim, Y.T., Prabhu, N., Dai, L., Go, K.D., Chen, D., Sreekumar, L., Egeblad, L., Eriksson, S., Chen, L., Veerappan, S., et al. (2018). An efficient proteome-wide strategy for discovery and characterization of cellular nucleotide-protein interactions. PLoS One *13*, e0208273.

Lin, A., Giuliano, C.J., Palladino, A., John, K.M., Abramowicz, C., Yuan, M. Lou, Sausville, E.L., Lukow, D.A., Liu, L., Chait, A.R., et al. (2019). Off-target toxicity is a common mechanism of action of cancer drugs undergoing clinical trials. Sci. Transl. Med. *11*, eaaw8412.

Longley, D.B., Harkin, D.P., and Johnston, P.G. (2003). 5-Fluorouracil: mechanisms of action and clinical strategies. Nat. Rev. Cancer *3*, 330–338.

Luengo, A., Gui, D.Y., and Vander Heiden, M.G. (2017). Targeting metabolism for cancer therapy. Cell Chem. Biol. *24*, 1161–1180.

Maraia, R.J., and Intine, R.V. (2002). La protein and its associated small nuclear and nucleolar precursor RNAs. Gene Expr. *10*, 41–57.

Marin-Vicente, C., Lyutvinskiy, Y., Romans Fuertes, P., Zubarev, R.A., and Visa, N. (2013). The effects of 5-fluorouracil on the proteome of colon cancer cells. J. Proteome Res. *12*, 1969–1979.

McGuigan, A., Kelly, P., Turkington, R.C., Jones, C., Coleman, H.G., and McCain, R.S. (2018). Pancreatic cancer: a review of clinical diagnosis, epidemiology, treatment and outcomes. World J. Gastroenterol. *24*, 4846–4861.

Meyer, C., Garzia, A., Mazzola, M., Gerstberger, S., Molina, H., and Tuschl, T. (2018). The TIA1 RNA-binding protein family regulates EIF2AK2-mediated stress response and cell cycle progression. Mol. Cell *69*, 622–635.e6.

Michaelis, M., Rothweiler, F., Barth, S., Cinat, J., Van Rikxoort, M., Löschmann, N., Voges, Y., Breitling, R., Von Deimling, A., Rödel, F., et al. (2011). Adaptation of cancer cells from different entities to the MDM2 inhibitor nutlin-3 results in the emergence of p53-mutated multi-drug-resistant cancer cells. Cell Death Dis. *2*, e243.

Michaelis, M., Wass, M.N., and Cinatl, J. (2019). Drug-adapted cancer cell lines as preclinical models of acquired resistance. Cancer Drug Resist. *2*, 447–456.

Mohni, K.N., Wessel, S.R., Zhao, R., Wojciechowski, A.C., Luzwick, J.W., Layden, H., Eichman, B.F., Thompson, P.S., Mehta, K.P.M., and Cortez, D. (2019). HMCES maintains genome integrity by shielding abasic sites in single-strand DNA. Cell *176*, 144–153.e13.

Molina, D.M., Jafari, R., Ignatushchenko, M., Seki, T., Larsson, E.A., Dan, C., Sreekumar, L., Cao, Y., and Nordlund, P. (2013). Monitoring drug target engagement in cells and tissues using the cellular thermal shift assay. Science *341*, 84–87.

Nakano, J., Huang, C., Liu, D., Masuya, D., Nakashima, T., Yokomise, H., Ueno, M., Wada, H., and Fukushima, M. (2006). Evaluations of biomarkers associated with 5-FU sensitivity for non-small-cell lung cancer patients postoperatively treated with UFT. Br. J. Cancer *95*, 607–615.

Pan, X., Zhang, X., Sun, H., Zhang, J., Yan, M., and Zhang, H. (2013). Autophagy inhibition promotes 5-fluorouraci-induced apoptosis by stimulating ROS formation in human non-small cell lung cancer A549 cells. PLoS One *8*, e56679.

Penzo, M., Guerrieri, A.N., Zacchini, F., Trer, D., and Montanaro, L. (2017). RNA pseudouridylation in physiology and medicine: for better and for worse. Genes (Basel) *8*, 301.

Prabhu, N., Dai, L., and Nordlund, P. (2020). CETSA in integrated proteomics studies of cellular processes. Curr. Opin. Chem. Biol. *54*, 54–62.

Qiu, L.-X., Tang, Q.-Y., Bai, J.-L., Qian, X.-P., Li, R.-T., Liu, B.-R., and Zheng, M.-H. (2008). Predictive value of thymidylate synthase expression in advanced colorectal cancer patients receiving fluoropyrimidine-based chemotherapy: evidence from 24 studies. Int. J. Cancer *123*, 2384–2389.

Riley, T., Sontag, E., Chen, P., and Levine, A. (2008). Transcriptional control of human p53-regulated genes. Nat. Rev. Mol. Cell Biol. *9*, 402–412.

Rodrigues, D., Souza, T., Jennen, D.G.J., Lemmens, L., Kleinjans, J.C.S., and de Kok, T.M. (2019). Drug-induced gene expression profile changes in relation to intestinal toxicity: state-of-the-art and new approaches. Cancer Treat. Rev. *77*, 57–66.

Sakamoto, K., Yokogawa, T., Ueno, H., Oguchi, K., Kazuno, H., Ishida, K., Tanaka, N., Osada, A., Yamada, Y., Okabe, H., et al. (2015). Crucial roles of thymidine kinase 1 and deoxyUTPase in incorporating the antineoplastic nucleosides trifluridine and 2′-deoxy-5-fluorouridine into DNA. Int. J. Oncol. *46*, 2327–2334.

Sánchez, A., Sharma, S., Rozenzhak, S., Roguev, A., Krogan, N.J., Chabes, A., and Russell, P. (2012). Replication fork collapse and genome instability in a deoxycytidylate deaminase mutant. Mol. Cell. Biol. *32*, 4445–4454.

Sasada, S., Miyata, Y., Tsutani, Y., Tsuyama, N., Masujima, T., Hihara, J., and Okada, M. (2013). Metabolomic analysis of dynamic response and drug resistance of gastric cancer cells to 5-fluorouracil. Oncol. Rep. *29*, 925–931.

Showalter, S.L., Showalter, T.N., Witkiewicz, A., Havens, R., Kennedy, E.P., Hucl, T., Kern, S.E., Yeo, C.J., and Brody, J.R. (2008). Evaluating the drug-target relationship between thymidylate synthase expression and tumor response to 5-fluorouracil: is it time to move forward? Cancer Biol. Ther. *7*, 986–994.

Sobrero, A.F., Aschele, C., and Bertino, J.R. (1997). Fluorouracil in colorectal cancer - a tale of two drugs: implications for biochemical modulation. J. Clin. Oncol. *15*, 368–381.

Sun, W., Dai, L., Yu, H., Puspita, B., Zhao, T., Li, F., Tan, J.L., Lim, Y.T., Chen, M.W., Sobota, R.M., et al. (2019). Monitoring structural modulation of redox-sensitive proteins in cells with MS-CETSA. Redox Biol. *24*, 101168.

Taylor, P.C., Balsa Criado, A., Mongey, A.-B., Avouac, J., Marotte, H., and Mueller, R.B. (2019). How to get the most from methotrexate (MTX) treatment for your rheumatoid arthritis patient?—MTX in the treat-to-target strategy. J. Clin. Med. *8*, 515.

Thompson, P.S. (2019). Protection of abasic sites during DNA replication by a stable thiazolidine protein-DNA crosslink. Nat. Struct. Mol. Biol *26*, 613–618.

Tieng, F.Y.F., Baharudin, R., Abu, N., Mohd Yunos, R.I., Lee, L.H., and Ab Mutalib, N.S. (2020). Single cell transcriptome in colorectal cancer—current updates on its application in metastasis, chemoresistance and the roles of circulating tumor cells. Front. Pharmacol. *11*, 135.

Tseng, W.C., Medina, D., and Randerath, K. (1978). Specific inhibition of transfer RNA methylation and modification in tissues of mice treated with 5-fluorouracil. Cancer Res. *38*, 1250–1257.

Vodenkova, S., Buchler, T., Cervena, K., Veskrnova, V., Vodicka, P., and Vymetalkova, V. (2020). 5-Fluorouracil and other fluoropyrimidines in colorectal cancer: past, present and future. Pharmacol. Ther. *206*, 107447.

Zhang, N., Yin, Y., Xu, S.J., and Chen, W.S. (2008). 5-Fluorouracil: mechanisms of resistance and reversal strategies. Molecules *13*, 1551–1569.

Zhao, X., and Yu, Y.T. (2007). Incorporation of 5-fluorouracil into U2 snRNA blocks pseudouridylation and pre-mRNA splicing in vivo. Nucleic Acids Res. *35*, 550–558.

STAR★METHODS

KEY RESOURCE TABLE

REAGENT or RESOURCE	SOURCE	IDENTIFIER
Antibodies		
Anti-TYMS (F-7) mouse mAb	Santa Cruz	Cat#sc-376161; RRID: AB_10989925
Anti-TYMS rabbit pAb	Proteintech	Cat#15047-1-AP; RRID: AB_2210721
Anti-DUT rabbit pAb	Proteintech	Cat#13740-1-AP; RRID: AB_2093170
Anti-HMCES rabbit pAb	Sigma	Cat#HPA044968; RRID: AB_2679160
Anti-PUS1 pAb	Sigma	Cat#HPA057593; RRID: AB_2683479
Anti-SOD1 rabbit pAb	Sigma	Cat#HPA001401; RRID: AB_1080132
Anti-p53 mouse mAb	Santa Cruz	Cat#sc-126; RRID: AB_628082
Anti-MDM2 mAb	Oncogene	Cat#2A9
Anti-p21 mouse mAb	Cell Signaling	Cat#2946; RRID: AB_2260325
Anti-rabbit IgG HRP-conjugated secondary antibody	Promega	Cat#W401B;RRID: AB_430833
Biological samples		
MCF7 (HTB-22, ATCC) breast cancer xenografts	Provided by collaborators at the Department of Microbiology, Tumor and Cell Biology (MTC), Karolinska Institute	N/A
Chemicals, peptides, and recombinant proteins		
DMEM high glucose medium	Sigma	Cat#D6429
McCoy's 5A medium	Sigma	Cat#M9309
RPMI-1640 medium	Sigma	Cat#R8758
F-12K Nut Mix (1x) medium	Gibco	Cat#21127-022
Heat-inactivated fetal bovine serum (FBS)	Gibco	Cat#10500-064
Penicillin-Streptomycin-Neomycin antibiotic mixture	Gibco	Cat#15640055
MEM Non-Essential Amino Acids	Gibco	Cat#11140050
L-Glutamine	Gibco	Cat#25030081
HBSS –CaCl2/–MgCl2	Gibco	Cat#14175-053
HBSS +CaCl2/+MgCl2	Gibco	Cat#14025-050
TrypLE Select (1X)	Gibco	Cat#12563-029
FdUTP (100 mM in H_2O)	Jena Bioscience	Cat#NU-154L
FUMP (10 mM in H_2O)	Jena Bioscience	Cat#NU-146L
FdUMP	Sigma	Cat#F3503
Floxuridine (FUDR)	Selleck Chem	Cat#S1299
5-Fluorouracil (5-FU)	Selleck Chem	Cat#S1209
5-Fluorouridine (FUR)	Sigma	Cat#F5130
Halt™ Protease Inhibitor Cocktail, EDTA-Free (100 X)	Thermo Scientific	Cat#1861279
SUPERase●In™ RNase Inhibitor	Thermo Scientific	Cat#AM2694
Hydroxyethyl-piperazineethane-sulfonic acid buffer (HEPES)	GOLDBIO	Cat#H-400-1
Beta-glycerophosphate	Sigma	Cat#G9422
Sodium orthovanadate	Sigma	Cat#72060
Magnesium chloride	Sigma	Cat#M8266 and M4880
EDTA-free protease inhibitor cocktail	NACALAI TESQUE	Cat#25955-11
Resazurin sodium salt	Sigma	Cat#R7017
Triton X-100	Sigma	Cat#11332481001
Na_2HPO_4	Sigma	Cat#S7907

(*Continued on next page*)

Continued

REAGENT or RESOURCE	SOURCE	IDENTIFIER
NaH_2PO_4	Sigma	Cat#S5011
β-mercaptoethanol	Sigma	Cat#M6250
40mM 3-carboxyumbelliferyl β-D-galactopyranoside (CUG) substrate	Thermo Scientific	Part of cat#F2905
Na_2CO_3	Sigma	Cat#223503
AlphaLISA immunoassay buffer (10X)	Perkin Elmer	Cat#AL000F
Anti-mouse Alpha donor beads	Perkin Elmer	Cat#AS104D
Anti-rabbit AlphaLISA acceptor beads	Perkin Elmer	Cat#AL104M
NuPAGE™ LDS Sample Buffer (4X)	Thermo Scientific	Cat#NP0008
NuPAGE™ Sample Reducing Agent (10X)	Thermo Scientific	Cat#NP0009
NuPAGE™ MES SDS Running Buffer (20X)	Thermo Scientific	Cat#NP0002
Tris Buffered Saline with 0,05% Tween 20 (TBS-T)	Medicago	Cat#09-7510-100
Clarity™ Western ECL Substrate	BioRad	Cat#170-5061
Clarity Max™ Western ECL Substrate	BioRad	Cat#1705062
Phosphate-buffered saline (10X) pH 7.4, RNase-free	Thermo Scientific	Cat#AM9624
UltraPure™ DNase/RNase-Free distilled water	Thermo Scientific	Cat#10977035
TRIzol™ reagent	Thermo Scientific	Cat#15596026
Chloroform	Sigma	Cat#C2432
99.5% analytical grade ethanol	Solveco	Cat#1015
PureLink™ RNA Mini purification kit	Thermo Scientific	Cat#12183018A
RNase Zap™	Thermo Scientific	Cat#AM9780
Triethylammonium bicarbonate buffer (TEAB)	Sigma	Cat#T7408
Bond-Breaker™ TCEP Solution	Thermo Scientific	Cat#77720
2-chloroacetamide (CAA)	Sigma	Cat#C0267
Lys-C	Wako Chemicals Ltd	Cat#129-02541
SOLu-Trypsin	Sigma	Cat#EMS0004
TMT10PLEX isobaric label reagent set	Thermo Scientific	Cat#90110
Sera-Mag SpeedBeads carboxylate-modified particles (Hydrophobic)	GE Healthcare	Cat#65152105050250
Sera-Mag SpeedBeads magnetic-carboxylate modified particles (Hydrophilic)	GE Healthcare	Cat#45152105050250
LC-MS grade formic acid (FA)	Merck	Cat#533002
LC-MS grade H_2O	Merck	Cat#115333
LC-MS hypergrade acetonitrile (ACN)	Merck	Cat#100029
LC-MS grade acetic acid	Merck	Cat#533001
Trifluoroacetic acid (TFA)	Sigma	Cat#T6508
Critical commercial assays		
DC protein assay	BioRad	Cat#500-0116
Pierce™ BCA protein assay kit	Thermo Scientific	Cat#23225
Quant-iT™ microRNA assay kit	Thermo Scientific	Cat#Q32882
Deposited data		
Protein abundance (log2) data for MS-CETSA	This manuscript	Data S1 - Protein abundance all datasets
MS-CETSA raw data	ProteomeXchange via the jPOST repository	http://proteomecentral.proteomexchange.org/Dataset identifiers PXD026470, PXD026471, and PXD026472

(*Continued on next page*)

Continued

REAGENT or RESOURCE	SOURCE	IDENTIFIER
Experimental models: Cell lines		
MCF7	ATCC	ID#HTB-22
Panc-1	ATCC	ID#CRL-1469
A549	ATCC	ID#CCL-185
HCT116	ATCC	ID#CCL-247
HCT15_Parental and HCT15_Resistant	Available from Resistant Cancer Cell Line (RCCL) collection	N/A
ARN8 (with a stably integrated p53-dependent β-galactosidase reporter construct)	Provided by collaborators at the p53Lab (A*STAR)	N/A
Experimental models: Organisms/strains		
NOD-SCID IL2R gamma null (NOG)	Animal facility at the Department of Microbiology, Tumor and Cell Biology (MTC), Karolinska Institute	N/A
Software and algorithms		
ImageLab™ software	BioRad	https://www.bio-rad.com/
Xcalibur v.4.0	Thermo Scientific	https://www.thermofisher.com/us/en/home.html
Proteome Discoverer v.2.1.0.81	Thermo Scientific	https://www.thermofisher.com/us/en/home.html
Mascot 2.6.0	Matrix Science	http://www.matrixscience.com
Sequest HT	Thermo Scientific	https://www.thermofisher.com/us/en/home.html
RStudio v.1.2.5033	RStudio	https://www.rstudio.com
R v.3.6.3	The R Foundation	https://www.r-project.org/
mineCETSA package	Dziekan et al. (2020); Lim et al. (2018)	https://github.com/nkdailingyun/mineCETSA
vsn package v3.54.0	Bioconductor	https://www.bioconductor.org/
ggplot2 package v.3.3.0	R CRAN	https://cran.r-project.org/
Cytoscape 3.7.2	Cytoscape	http://cytoscape.org
ClueGO v2.5.1	Cytoscape	http://apps.cytoscape.org/apps/cluego
GraphPad Prism v.8.3.0	GraphPad Software	https://www.graphpad.com/
Other		
Falcon® 150cm^2 cell culture flask	Corning	Cat#355001
Falcon® 75cm^2 cell culture flask	Corning	Cat#353136
Falcon® 25cm^2 cell culture flask	Corning	Cat#353109
384-well AlphaPlates	PerkinElmer	Cat#6008350
96-well plates (black)	Greiner	Cat#655090
NuPAGE 4–12% Bis-Tris midi gel	Invitrogen	Cat#WG1403BX10
iBlot 2 NC regular stacks	Invitrogen	Cat#IB23001
Non-fat milk powder	Semper AB	N/A
Oasis HLB 1cc (10mg) extraction cartridges	Waters	Cat#186000383
Xbridge Peptide BEH C18, 300 Å, 3.5 μm, 2.1 mm × 250 mm column	Waters	Cat#186003610
Zorbax 300 Extend C-18 4.6 mm × 250 mm column	Agilent	Cat#770995-902
50 cm x 75 μm(ID) EASY-Spray analytical column	Thermo Scientific	Cat#ES803
Veriti™ 96-Well thermal cycler	Applied Biosystems	P/N 4375786
EnSpire plate reader	Perkin Elmer	P/N 2300
Tecan Infinite Pro plate reader	Life Sciences	P/N 30063849

(*Continued on next page*)

Continued

REAGENT or RESOURCE	SOURCE	IDENTIFIER
Nanodrop2000	Thermo Scientific	Cat#ND-2000
XCell4 SureLock™ Midi-Cell	Invitrogen	Cat#WR0100
iBlot 2 system	Invitrogen	Cat#IB21001
ChemiDoc™ XRS+ imaging system	BioRad	Universal Hood III
SpeedVac vacuum concentrator	Thermo Scientific	P/N SPD111V-230, 61010-1, and RV5 A65313906
ÄKTA Micro system	GE Healthcare	Cat#28948303
Dionex UltiMate 3000 UPLC system	Thermo Scientific	P/N 5041.0010, 5826.0020, and 5035.9245
Q Exactive HF mass spectrometer	Thermo Scientific	Cat#IQLAAEGAAPFALGMBFZ

RESOURCE AVAILABILITY

Lead contact

Further information and requests for resources and reagents should be directed to and will be fulfilled by the lead contact, Pär Nordlund (par.nordlund@ki.se).

Materials availability

The 5-FU-resistant HCT15 cells generated in this study are available from Resistant Cancer Cell Line (RCCL) collection (Michaelis et al., 2019).

Data and code availability

The extracted protein abundance data from all MS-CETSA experiments are included in supplemental "Data S1 - Protein abundance all datasets".

All mass spectrometry raw data files have been deposited to the ProteomeXchange Consortium (http://proteomecentral.proteomexchange.org/) via the jPOST repository with the dataset identifiers PXD026470, PXD026471, and PXD026472. Any additional information required to reanalyse the data reported in this paper is available from the lead contact upon request.

EXPERIMENTAL MODEL AND SUBJECT DETAILS

Cell lines

Several cancer cell lines of human origin were purchased from ATCC: MCF7 (HTB-22, derived from pleural effusion at the metastatic site of a 69 year old female with breast adenocarcinoma), Panc-1 (CRL-1469, established from tumour tissue surgically removed from a 56 year old male with pancreatic/duct epithelioid carcinoma), A549 (CCL-185, established from tumour tissue surgically removed from a 58 year old male with lung carcinoma), HCT116 (CCL-247, established from a tumour sample collected from an adult male with colorectal carcinoma). The HCT-15 cell line was purchased from DSMZ (Braunschweig, Germany). The HCT-15 subline adapted to growth in the presence of 2,000 ng/mL 5-FU (HCT-15^{r}5FU^{2000}) was established by continuous exposure to step-wise increasing drug concentrations as previously described (Kotchetkov et al., 2005; Michaelis et al., 2011) and derived from the Resistant Cancer Cell Line (RCCL) collection (Michaelis et al., 2019). The human melanoma cell line ARN8, containing a stably integrated, p53-dependent β-galactosidase reporter construct, was kindly provided by David P. Lane's Group of the p53Lab (A*STAR).

MCF7, ARN8 and Panc-1 cells were cultured in DMEM high glucose medium (D6429, Sigma), supplemented with 10% heat-inactivated fetal bovine serum (FBS) (10500-064, Gibco), A549 in F-12K Nut Mix (1×) medium (21127-022, Gibco) supplemented with 10% FBS, and HCT116 in McCoy's 5A medium (M9309, Sigma) supplemented with 10% FBS. HCT15_Parental and HCT15_Resistant cells were maintained in RPMI-1640 medium (R8758, Sigma), 1× Penicillin-Streptomycin-Neomycin (PSN) antibiotic mixture (15640055, Gibco), 1× MEM Non-Essential Amino Acids (11140050, Gibco) and L-Glutamine (25030081, Gibco), and without or with 16μM 5-FU, respectively. For cell passaging, cells were washed with HBSS–$CaCl_2$/–$MgCl_2$ (14175-053, Gibco) and detached by 3 minutes incubation with TrypLE Select 1× (12563-029, Gibco) at 37°C.

Mouse models

All mouse studies were approved by the Northern Stockholm Experimental Animal Ethical Committee (Dnr. N 192/13 and Dnr. N 2/17) and were performed at the animal facility at Department of Microbiology, Tumor and Cell Biology (MTC), Karolinska Institute in strict compliance with the guidelines and regulations established by the Northern Stockholm Experimental Animal Ethical Committee as well as institutional guidelines established by Karolinska Institute.

NOD-SCID IL2R gamma null (NOG) mice were obtained from the breeding unit at MTC, Karolinska Institute. NOG mice were bred in individually ventilated cages (IVCs) at the breeding unit at MTC, Karolinska Institute. MCF7 (ATCC, HTB-22; RRID: CVCL_0031) xenograft tumour growth was initiated by injecting with 5 ×10^6 MCF7 cells into the lower-right mammary gland of 7-9 weeks old NOG

females. The MCF7 xenograft tumours were allowed to grow for approximately 60 days until the tumours reached approximately 1.0 cm^3 in size. Tumour volumes were measured with a caliper and calculated according to the formula: volume = length- × $width^2$ × 0.52. Up to five mice were housed in an IVC cage.

METHOD DETAILS

The cellular thermal shift assay (CETSA)

CETSA in cell lysate

FdUTP (NU-154L, Jena Bioscience, 100 mM in H_2O) and FUMP (NU-146L, Jena Bioscience, 10 mM in H_2O) stocks were purchased from Jena Bioscience. FdUMP (F3503, Sigma) was resuspended in sterile MilliQ H_2O at 100 mM. All compound stocks were aliquoted and stored at -80°C.

MCF7 cells were harvested, washed in HBSS+$CaCl_2$/+$MgCl_2$ (14025-050, Gibco), centrifuged for 3 min at 300×g, and resuspended in HBSS+$CaCl_2$/+$MgCl_2$ at a cell density of 40 ×10^6 cells/mL. The cells were subjected to 3× freeze-thawing cycles in the presence of 1× Halt™ protease inhibitor cocktail (1861279, Thermo Scientific), with vortexing in between the cycles, followed by 20 min centrifugation at 20 000×g at 4°C. The supernatant (clarified lysate) was collected and directly used for experiments. For the CETSA experiments, clarified lysate was mixed in PCR tubes with either drugs or vehicle and incubated at RT for 2 min. CETSA heating was immediately performed for 3 min at the selected temperatures in a Veriti thermal cycler (Applied Biosystems), followed by a 3 min cooling step at RT. The soluble protein fraction was isolated by 20 min centrifugation at 20 000 ×g at 4°C. The samples were diluted 2× in HBSS+$CaCl_2$/+$MgCl_2$ prior to preparation for western blot analysis. All work with cell lysate was performed on ice.

CETSA in intact cells

FUDR (S1299, Selleck Chem) and FUR (F5130, Sigma) were solubilised at 50 mM in H_2O. 5-FU (S1209, Selleck Chem) was solubilised at 50 mM in DMSO. All compound stocks were aliquoted and stored at -80°C.

CETSA melt curves

For the *in vitro* melt curve experiments, cells were seeded in sterile T75 cell culture flasks (353136, Falcon™) in the appropriate complete medium and incubated for approximately 24 hours to 80% confluency at 37°C and 5% CO_2. Next, the cells were treated with either drug or vehicle diluted in the appropriate medium supplemented with 5% heat inactivated FBS, and incubated at 37°C and 5% CO_2. The cells were briefly washed in HBSS–$CaCl_2$/–$MgCl_2$, detached from the flask using TrypLE, collected in HBSS +$CaCl_2$/+$MgCl_2$, pelleted for 3 min at 300×g and resuspended in HBSS+$CaCl_2$/+$MgCl_2$. The cells were then aliquoted into PCR tubes then heated in a Veriti thermal cycler (Applied Biosystems) for 3 min at different temperatures. The samples were then subjected to 3 cycles of freeze-thawing in liquid nitrogen in the presence of 1× Halt™ protease inhibitor cocktail (1861279, Thermo Scientific). Samples were centrifuged at 20 000g for 20 min at 4°C and soluble protein extract was used for further analysis.

$ITDR_{CETSA}$

For the *in vitro* $ITDR_{CETSA}$ cell experiments, cells were seeded in sterile T25 cell culture flasks (353109, Falcon™) in the appropriate complete medium at a cell density that would result in a 80% confluency, then treated with either vehicle or different concentrations of 5-FU in the appropriate medium supplemented with 5% heat inactivated FBS, and incubated for 12h at 37°C and 5% CO_2. The final DMSO concentration in all treatment conditions was 0.4%. Next, the cells were washed in HBSS –$CaCl_2$/–$MgCl_2$, detached from the flasks using TrypLE, collected in HBSS +$CaCl_2$/+$MgCl_2$, pelleted by centrifugation for 3 min at 300×g, resuspended in HBSS +$CaCl_2$/+$MgCl_2$, and aliquoted into PCR tubes. A CETSA heating step of 3 minutes at several preselected temperatures was performed in a Veriti thermal cycler (Applied Biosystems). The samples were then subjected to 3 cycles of freeze-thawing in liquid nitrogen in the presence of 1× Halt™ protease inhibitor cocktail (1861279, Thermo Scientific). The soluble protein fraction was isolated by centrifugation for 20 min at 20 000×g at 4°C. Protein concentration in each sample was determined using the DC protein assay (500-0116, BioRad) according to the manufacturer's protocol. Equal amounts of total protein from each sample were analysed using western blotting.

IMPRINTS-CETSA

For the *in vitro* IMPRINTS-CETSA experiments, cells were seeded in T75 cell culture flasks (353136, Falcon™) in the appropriate complete medium at a cell density that would result in 80% confluency. The cells were then treated with either drug or vehicle diluted in the appropriate medium supplemented with 5% heat-inactivated FBS, and incubated at 37°C and 5% CO_2. Next, the cells were briefly washed in HBSS –$CaCl_2$/–$MgCl_2$, detached from the flask using TrypLE, collected in HBSS +$CaCl_2$/+$MgCl_2$, pelleted for 3 min at 300×g, and resuspended in HBSS +$CaCl_2$/+$MgCl_2$. The cells corresponding to each treatment condition were aliquoted into PCR tubes then heated in a Veriti thermal cycler (Applied Biosystems) for 3 min at 6 different temperatures (37°C, 47°C, 50°C, 52°C, 54°C, 57°C). After heating, all samples were subjected to 3 cycles of freeze-thawing in liquid nitrogen in the presence of 1× Halt™ protease inhibitor cocktail (1861279, Thermo Scientific). For the HCT15_Parental and HCT15_Resistant cells, lysis was performed in 1× kinase buffer containing 50mM HEPES, pH 7.5, 5mM beta-glycerophosphate (G9422, Sigma), 0.1mM sodium orthovanadate (Na_3VO_4) (72060, Sigma), 10mM $MgCl_2$ (M8266, Sigma), and 1× protease inhibitor (NACALAI TESQUE, 25955-11), and lysed by multiple rounds of freeze-thawing in combination with mechanical shearing. The soluble protein fraction was isolated by 20 min centrifugation at 20 000×g at 4°C, and analysed using either LC-MS or western blotting.

CETSA in mouse models

For the *in vivo* CETSA experiments 5-FU (S1209, Selleck Chem) was solubilised at 45 mg/mL in 84.7 mg/mL Tris base in sterile MilliQ H_2O. The 5-FU stock solution was subsequently diluted in 84.7 mg/mL Tris base, so that mice would be administered 100 μL of the designated 5-FU solution in order for the final dose to be achieved. All compound solutions were prepared fresh, prior to treating the mice. Five MCF7 xenograft-bearing mice of similar size were treated intravenously with either vehicle or different 5-FU doses (10, 50, 100, and 150 mg/kg). After the treatment, each mouse was singly kept in the IVC until euthanasia. The mice were euthanised 22 hours after treatment. The grafted tumours were excised and placed in 15 mL tubes on ice until further processing. Each xenograft tumour was cut in similar-sized pieces using a scalpel transferred to PCR tubes containing HBSS +$CaCl_2$/+$MgCl_2$ and 1× Halt™ protease inhibitor cocktail (1861279, Thermo Scientific). The samples intended for AlphaLISA readout were then heated at 8 different temperatures (37-72°C in duplicates), while the samples for MS-CETSA were heated at 37°C and 52°C (triplicates for each temperature). Following the CETSA heating, the samples were subjected to 3 cycles of freeze-thawing using liquid nitrogen. Further homogenisation was done by mechanically shearing the tumour pieces in their tubes using a spatula. The soluble protein extracts were separated from the protein aggregates and cell debris by centrifugation at 20000×g, 20 minutes at 4°C. The supernatants were collected and analysed using either AlphaLISA or LC-MS.

Cell proliferation and viability assays

For assessment of 5-FU cytotoxicity, MCF7, A549, Panc-1, HCT116, HCT15 Parental, or HCT15 Resistant cells in their respective complete media were seeded in black 96-well polystyrene plates with clear bottom (Sigma) at a cell density optimal for each cell line (predetermined). The cells were first incubated for 24h at 37°C and % CO_2 in order to adhere to the plate and resume log-phase growth, then treated with either vehicle (DMSO) or respective compound diluted in the corresponding media supplemented with 5% heat inactivated FBS for the indicated duration. The final DMSO concentration was 0.4% in all wells. 10 μg/mL resazurin sodium salt (R7017, Sigma) was added to each well and further incubation was carried out for 2h. Fluorescence was measured at 590 nm using an EnSpire plate reader (Perkin Elmer).

AlphaLISA

Soluble protein extracts were transferred in duplicates to 384-well AlphaPlates (6008350, PerkinElmer) along with a master mix containing anti-thymidylate synthase (TYMS) antibodies, AlphaLISA donor and acceptor beads in AlphaLISA immunoassay buffer (#AL000F, PerkinElmer) diluted to 1x in HBSS +$CaCl_2$/+$MgCl_2$. The final concentrations for the assay reagents were: 0.4 nM mouse monoclonal anti-TYMS (sc-376161, Santa Cruz Biotechnology), 1 nM rabbit polyclonal anti-TYMS (15047-1-AP, Proteintech), 40 μg/mL anti-mouse donor beads (AS104D, Perkin Elmer), 10 μg/mL anti-rabbit AlphaLISA acceptor beads (AL104M, Perkin Elmer). The plates were sealed and protected from light, centrifuged briefly at 200×g, and incubated overnight at RT in the dark. The next day, the plates were centrifuged briefly at 200×g and 1 min, and read in an EnSpire plate reader (Perkin Elmer) using the default AlphaLISA readout settings. All work with AlphaLISA beads was done under subdued green (LEE 090-filtered) light conditions.

p53-activation reporter assay

ARN8 stable cells (derived from human melanoma A375 cells and expressing lacZ with a p53 responsive element) were seeded 24h prior treatment in a black 96-well plate (655090, Greiner) at a density of 8000 cells/well. Medium was replaced by respective medium containing appropriate drug concentrations, positive or negative control. Cells were treated in triplicates and incubated at 37°C for 22h. Subsequently the medium was removed, cells were washed once with PBS and 100μl lysis buffer (0.1% Triton X-100 (11332481001, Sigma)) in reaction buffer (0.1M Sodium phosphate pH 7.3 (S7907 and S5011, Sigma), 1mM $MgCl_2$ (M4880, Sigma), 45mM β-mercaptoethanol (M6250, Sigma)) was added into each well for 30-45min. 1.1mM CUG substrate (part of F2905, Thermo Scientific) was added and incubated for 30min at RT, followed by termination of reaction with 50μl 0.2M Na_2CO_3 stop solution (223503, Sigma). The fluorescence was measured at 390nm excitation and 460nm emission using a Tecan infinite Pro plate reader (LifeSciences).

RNA isolation and quantification

HCT15_Parental and HCT15_Resistant cells were seeded in T150 cell culture flasks (355001, Falcon™) in the appropriate complete medium at a cell density that would result in 80% confluency. The cells were then treated with either 100 μM 5-FU or vehicle diluted in the appropriate complete medium and incubated for 12h at 37°C and 5% CO_2. Next, the cells were briefly washed in HBSS –$CaCl_2$/–$MgCl_2$, detached from the flask using TrypLE, collected in RNase-free 1× PBS in H_2O (AM9624 and 10977035, Thermo Scientific), pelleted for 3 min at 300×g, and resuspended at equal cell densities in 1× PBS in RNase-free H_2O containing 1× Halt™ protease inhibitor cocktail (1861279, Thermo Scientific) and SUPERase•In™ RNase Inhibitor (AM2694, Thermo Scientific). The samples were then subjected to 3 cycles of freeze-thawing in liquid nitrogen and the cell lysates were clarified by centrifugation at 10 000×g for 10 min at 4°C. Protein concentration in the clarified lysates was determined using the DC protein assay (500-0116, BioRad) according to the manufacturer's protocol. For RNA isolation, equal amounts of clarified cell lysate from each sample (100 μL from clarified lysate at 1 mg total protein/mL) were mixed with 900 μL TRIzol™ reagent (15596026, Thermo Scientific) and incubated at RT for 5 minutes. 200 μL chloroform (C2432, Sigma) were added to each sample, followed by inverting the tubes several times and 5 min incubation at RT. The samples were then centrifuged for 15 min at 12 000×g at 4°C and the aqueous phase was collected in separate tubes, mixed with 99.5% analytical grade ethanol (1015, Solveco) to a final ethanol concentration of 75%, and incubated at RT for 20 min. The

RNA in the samples was purified using the PureLink™ RNA Mini purification kit (12183018A, Thermo Scientific) following the manufacturer's instructions for total transcriptome isolation using the TRIzol™ reagent. In short, the RNA samples were passed through spin cartridges supplied with the PureLink™ RNA Mini purification kit, washed 2× with the supplied wash buffer II, and eluted with 30 μL RNAse-free H_2O in two consecutive steps. RNA concentration in the eluates was determined using the Quant-iT™ microRNA assay kit (Q32882, Thermo Scientific) and with a Nanodrop2000 spectrophotometer. All RNA-isolation and quantification experiments were conducted in a sterile biosafety cabinet class II. RNase-free laboratory consumables were used and RNase Zap™ (AM9780, Thermo Scientific) was used on all surfaces involved.

Western blot

Soluble protein extract samples were mixed with NuPAGE loading buffer consisting of NuPAGE LDS sample buffer (NP0008, Life technologies) and reducing agent (NP0009, Life Technologies). Proteins were separated on NuPAGE 4–12% Bis-Tris midi gels (WG1403BX10, Invitrogen) for 45-55 min at 200 V. Separated proteins were transferred to nitrocellulose membranes using the iBlot2 system (Invitrogen) and iBlot 2 NC Regular Stacks (IB23001, Invitrogen). Membranes were blocked in 5% (w/v) non-fat milk (Semper AB) in TBS with 0.05% Tween 20 (Medicago 09-7510-100) (TBS-T) for 1 h with gentle shaking. Incubation with primary antibody was performed overnight at 4°C and with gentle shaking. After washing in TBS-T for 3×10 min, the membranes were incubated with secondary antibodies for 1 h, washed again 3×10 min in TBS-T and developed using either Clarity™ Western ECL Substrate (170-5061, BioRad) or Clarity Max™ Western ECL Substrate (1705062, BioRad). All antibodies were prepared in 5% (w/v) non-fat milk in TBS-T at the dilutions listed below. The chemiluminescent signal was detected using the ChemiDoc™ XRS+ imaging system from BioRad and the band intensities were quantified using ImageLab™ software (BioRad).

Primary antibodies: 1:1000 anti-TYMS (15047-1-AP, Proteintech), 1:1000 anti-HMCES (HPA044968, Sigma), 1:1000 anti-PUS1 (HPA057593, Sigma), 1:1000 anti-DUT (13740-1-AP, Proteintech), 1:20 000 anti-SOD1 (HPA001401, Sigma), 1:1000 anti-p53 (sc-126, SantaCruz), 1:1000 anti-MDM2 (2A9, Oncogene), 1:1000 anti-p21 (2946, CellSignaling). Secondary antibody 1:20 000 anti-rabbit (W401B, Promega).

Sample preparation for LC-MS

The FUDR/FUR in MCF7 cells IMPRINTS-CETSA samples were prepared for LC-MS and analysed at Karolisnka Institute, Stockholm, Sweden, while the 5-FU in parental and resistant HCT15 cells the IMPRINTS-CETSA samples were prepared and analysed at Nanyang Technological University, Singapore. Protein concentrations were determined in the samples using Pierce™ BCA Protein Assay Kit (Thermo Scientific) and equal amounts of total protein from each condition were used for sample preparation. Samples were dried and resuspended in 50 mM triethylammonium bicarbonate (TEAB) buffer (T7408, Sigma) in H_2O (LC-MS grade, 115333, Merck), reduced with 5 mM TCEP (77720, Bond-breaker™, Thermo Scientific) at 65°C for 30 min, followed by alkylation with 15mM 2-chloroacetamide (CAA) (C0267, Sigma) at 37°C in the dark. Digestion of the samples was performed with 1:50 Lys-C (Wako Chemicals Ltd) at 37°C for 2h, followed by 1:50 SOLu-Trypsin (EMS0004, Sigma) at 37°C overnight. After digestion efficiency was checked, the peptides were labelled with Isobaric Tandem Mass Tags (TMT)-10plex (90110, Thermo Scientific) at 37°C for 3h, followed by checking labelling efficiency (>95% TMT-labelled PSMs). Three biological replicates from the treatment conditions at the same temperature were labelled as a set. The labelled samples from the same TMT set were pooled and the labelling reaction was stopped by adding 10% trifluoroacetic acid (Sigma) to reach pH < 3. Samples were dried in a SpeedVac vacuum concentrator (Thermo Scientific) and desalted using Oasis HLB 1cc (10mg) extraction cartridges (186000383, Waters) according to manufacturer's protocol. For the FUDR/FUR IMPRINTS-CETSA samples, additional steps were performed, which consisted of cleaning using magnetic carboxylate-modified beads (Sera-Mag SpeedBeads carboxylate-modified particles (Hydrophobic), 65152105050250, GE Healthcare mixed 1:1 with SpeedBeads carboxylate-modified particles (Hydrophilic), 45152105050250, GE Healthcare), followed by an additional desalting step using Oasis HLB extraction cartridges. Offline pre-fractionation of the samples was performed by high pH reverse-phase liquid chromatography using the ÄKTA Micro system (GE Healthcare). A Xbridge Peptide BEH C18, 300 Å, 3.5 μm, 2.1 mm × 250 mm column (#186003610, Waters) was used for pre-fractionation at the Stockholm lab, and a Zorbax 300 Extend C-18 4.6 mm × 250 mm column (770995-902, Agilent) was utilised for pre-fractionation at the Singapore lab. The fractions were concatenated into 12 fractions (Stockholm lab) or 20 fractions (Singapore lab) and dried using a SpeedVac vacuum concentrator (Thermo Scientific).

LC-MS

The digested, labeled, and dried peptide sample fractions were resuspended in 0.1% FA (LC-MS grade, 533002, Merck) in H_2O (LC-MS grade, 115333 Merck) (Stockholm lab). Online chromatography was performed using Dionex UltiMate 3000 UPLC system coupled to a Q Exactive HF mass spectrometer (Thermo Scientific). Each fraction was separated on a 50 cm x 75 μm (ID) EASY-Spray analytical column (Thermo Scientific) in 70 min gradient of programmed mixture of solvent A (0.1% formic acid in H_2O) and solvent B (99.9% acetonitrile, 0.1% formic acid). MS data were acquired using a top 12 data-dependent acquisition method. Full scan MS spectra were acquired in the range of 375-1500 m/z at a resolution of 70,000 and AGC target of 3e6; Top 12 dd-MS^2 70,000 and 3e6 with isolation window at 1.2 m/z. For samples prepared in Singapore lab, dried peptide fractions were resuspended in 1% acetonitrile (LC-MS hypergrade, 100029, Merck), 0.5% (v/v) acetic acid (LC-MS grade, 533001, Merck) and 0.06% TFA in H_2O (Singapore lab) immediately before LC-MS analysis. Online chromatography was performed using Dionex UltiMate 3000 UPLC system coupled to a Q Exactive HF mass spectrometer (Thermo Scientific). Separation was performed on a 50 cm×75 μm EASY-Spray analytical column (Thermo Scientific) with a pre-programmed gradient by mixing solvent A (0.1% formic acid in water) and solvent B (0.1% formic acid in acetonitrile)

over 70 min. MS data was acquired using a top 12 data-dependent acquisition method. Full scan MS spectra were acquired in the range of 350-1550 m/z at a resolution of 60,000 and AGC target of 3e6; Top 12 dd-MS2 45,000 and 1e5 with isolation window at 1.0 m/z.

QUANTIFICATION AND STATISTICAL ANALYSIS

Protein identification and quantification

Protein identification was performed by Proteome Discoverer 2.1 software (Thermo Scientific), using Mascot 2.6.0 (Matrix Science) and Sequest HT (Thermo Scientific) search engines to search against reviewed human Uniprot database (downloaded on 13 Jan 2017, including 42105 sequence entries). MS precursor mass tolerance was set at 20ppm, fragment mass tolerance 0.05 Da, and maximum missed cleavage sites of 2. Dynamic modifications searched for Oxidation (M), Deamidation (NQ), and Acetyl N-terminal protein. Static modifications: Carbamidomethyl (C) and TMT10plex (K and peptide N terminus). Only the spectrum peaks with signal-to-noise ratio (S/N) > 4 were chosen for searches. The false discovery rate (FDR) was set to 1% at both PSM and protein group levels. Only the unique and razor peptides were used for protein assignment and abundance quantification. Isotopic correction of the reporter ions in each TMT channel was performed according to the product sheet. Only the master proteins in the protein group were used for downstream analysis.

Quantitative MS data analysis and visualisation

Quantified protein abundances were imported into the R environment (http://www.R-project.org/) to facilitate the data analysis and visualisation. Data cleaning, normalisation, and calculations of protein abundance and thermal stability differences in each condition were performed using our in-house developed mineCETSA package (Dziekan et al., 2020; Lim et al., 2018). Strict criteria for hit selection were applied for all datasets. For the *in vivo* mouse ITDR dataset we required that the sigmoidal curve fitting (R^2 value) should be greater than 0.8. Additionally, a minimum responsive level of 1.3-fold change in the last three dose-points compared to the vehicle control should be exceeded in order for a protein to be considered a hit. Furthermore, hit calling requires a thermal shift at 52°C with a stable abundance signal at 37°C. For IMPRINTS-CETSA we require that proteins should be quantified by at least 2 peptide spectrum matches (PSMs) and have quantitative values in all six temperatures for hit selection. As cut-off criteria we used an absolute mean fold change and a standard error of the mean (SEM)-scale factor as cut-off. For IMPRINTS-CETSA experiments using 5-FU metabolites a mean log2 fold change cut-off > 0.25 and ± 5× SEM as compared to reference condition was applied. For experiments using parental and resistant HCT15 cells, a mean log2 fold change cut-off > 0.2 and ± 4× SEM was applied. When assessing expression level changes, only values from the 37°C condition were used for hit selection. Details regarding experimental replicates can be found in the figure legends.

Protein-protein interaction network and gene ontology (GO) enrichment analysis

Protein-protein interaction network for hits was obtained by importing a list of Uniprot IDs into Cytoscape v.3.7.2 (http://cytoscape.org). Using the embedded STRING interaction database (http://apps.cytoscape.org/apps/stringApp), a default confidence cut-off score of 0.4 was applied to retrieve the network. Each node represents one hit protein and edges symbolise protein-protein interactions. Colours of nodes indicate the treatment conditions that resulted in a protein hit. Comparative GO analysis was performed using the ClueGO v2.5.1 plug-in in Cytoscape (http://apps.cytoscape.org/apps/cluego). Uniprot IDs were imported to query the GO-Biological Processes database (EBI-QuickGO-GOA-15783 terms/pathways with 17268 available unique genes-20.11.2017). The parameters for analysis were set as follows: Evidence code – All; Use Go Term Fusion; GO tree interval – Level 3-8; GO Term/Pathway Selection – Minimum 3 genes and threshold of 4% of genes per term; GO term connectivity threshold (Kappa score) – 0.4; Two-sided hypergeometric test with Bonferroni step down p-value correction. Only GO terms with p-value <0.05 are shown. GO terms are presented as nodes and clustered together based on term similarity. Node size is proportional to the p-value for GO term enrichment. The node colour is set according to the treatment condition showing the % of visible proteins of a term/pathway.

Analysis and visualisation of melt curve MS-CETSA, $ITDR_{CETSA}$, and cell viability data

All graphs were generated using GraphPad Prism or in R environment. All data are presented as mean with error bars representing the standard error of the mean (SEM). Error bars that are smaller than the displayed data points are not displayed by the software. Details regarding replicates for each experiment can be found in the figure legends. Sigmoidal curves were fit (where appropriate) in GraphPad Prism using non-linear regression of the type [Inhibitor] versus Response (three parameters) with the function Y=Bottom + (Top-Bottom)/(1+(X/IC50)). $ITDR_{CETSA}$ data corresponding to vehicle-treated cells (0 μM) in Figures 5A–5C are depicted at 10^{-1} μM on the logarithmic scale. Cell viability data corresponding to vehicle-treated cells (0 μM) in Figure 5D are depicted at 10^{-3} μM on the logarithmic scale.

Correlation analysis

Data for correlation analysis for 5-FU sensitivity and expression levels were obtained from Cancer Dependancy Map (www.depmap.org) and further analysed and visualized in GraphPad Prism 9. Data was tested for normal distribution using Anderson-Darling test followed by unpaired, two-tailed t-test or Pearson correlation analysis. Statistical details for the analysis can also be found in the figures and figure legends.